Materials Advances

ROYAL SOCIETY OF CHEMISTRY

PAPER

View Article Online
View Journal | View Issue

Cite this: *Mater. Adv.*, 2024, 5, 762

DPP-bridged narrow band gap oligomer-like donor materials: significant effect of molecular structure regulation on photovoltaic performance†

Chang Liu, Lunxiang Yin,* Yanli Guo, Bao Xie, Xu Wang and Yanqin Li*

Narrow band gap oligomer-like materials with definite molecular structures have become a new trend in developing materials for the active layer of organic solar cells (OSCs). This is mainly because oligomer-like molecular donors (OMDs) have the structural characteristics of both small molecules and polymers. However, the degree of matching of the electron donor and acceptor units in oligomer-like molecules and the ability to push/pull electrons significantly affect the photoelectric properties of materials. Herein, the Suzuki coupling reaction was used to prepare a series of oligomer-like materials named **Flu(DPPFlu)$_2$**, **BPF(DPPBPF)$_2$**, **BPF(DPPCz)$_2$**, and **Cz(DPPCz)$_2$**. Density functional theory (DFT) calculations revealed the rationality of the molecule design in detail. The significant changes in the short circuit current (J_{sc}) and photoelectric conversion efficiency (PCE) of devices based on these oligomer-like materials are caused by three progressive optimization stages: side chain modification, end group strategy, and skeleton regulation, which prove that molecular engineering based on the oligomer-like skeleton can improve the photovoltaic performance of materials. It is worth mentioning that the oligomer-like molecule **Cz(DPPCz)$_2$** has achieved satisfactory regulation among these materials. The band gap significantly reduced to 1.32 eV and the PCE increased to 6.12% through the design scheme from small molecules to oligomer-like materials. More excitingly, the PCE of 6.12% based on the oligomer-like material is three times higher than that previously reported for the small molecule counterpart DPP(Cz)$_2$. This work provides an important reference for the future development of high-efficiency photovoltaic materials based on oligomer-like molecular structures.

Received 29th October 2023,
Accepted 27th November 2023

DOI: 10.1039/d3ma00925d

rsc.li/materials-advances

Introduction

Organic solar cells (OSCs) have emerged as highly promising candidates for converting solar energy into electricity owing to their distinctive advantages, including lightweight design, mechanical flexibility, diverse material options, and simplified device technology.[1] The efficient OSC employs a blend of donor (D) and acceptor (A) materials in the photoactive layer of bulk heterojunction (BHJ) devices, facilitating effective exciton dissociation and charge transfer.[1d] The donor material absorbs photons, generates excitons, and diffuses to the D–A interface, subsequently dissociating into carriers (electrons and holes) driven by the built-in electric field, which subsequently migrate to the electrode, resulting in the generation of photocurrent. The design and selection of the acceptor and donor materials have a significant impact on the photoelectric performance of devices, particularly with advancements in new materials.[2] $PC_{71}BM$ shows excellent light absorption characteristics and high electron affinity, so it has become a commercial acceptor material in OSC. In the past decade, the PCE of OSCs with $PC_{71}BM$ as the acceptor has reached 13–15%.[3] As donor materials for the photoactive layer, polymers have made great achievements, and PCE can exceed 19%.[4] On the one hand, conductive polymers greatly prolong the conjugation of molecules, broaden their optical absorption, reduce the band gap, and facilitate the capture of photons. On the other hand, polymer-based devices have solution processability and flexibility,[4f] which is more conducive to the formation of a network interpenetrating structure with acceptor molecules, thus improving exciton separation and charge transfer.[4a] Compared with polymer donor materials, small molecular donors (SMDs) have the advantages of definite molecular structure, high purity, easy modification and regulation of properties, good solubility, and diverse device processes. The optimized PCE can also exceed 15%.[5,6]

School of Chemistry, Dalian University of Technology, Dalian, 116024, China. E-mail: lxyin@dlut.edu.cn, liyanqin@dlut.edu.cn; Tel: +86-155-24572530

† Electronic supplementary information (ESI) available: synthesis, NMR spectra, MALDI-TOF HRMS, computational electronic transitions, Temperature dependent UV-vis properties of materials and surface tension data. See DOI: https://doi.org/10.1039/d3ma00925d

Many strategies can be used to control molecules' energy levels and band gaps to better match the acceptor materials.[6] However, as the active layer material of thin film devices, the film-forming property of small organic molecules is usually not as good as that of polymer materials.[7] Therefore, it is a challenge to balance the absorption range, band gap, crystallinity, and phase separation of the active layer material. The development of oligomers with intermediate molecular weights has facilitated the integration of the polymer and small molecule advantages, leading to significant advancements in the photoelectric conversion efficiency[8b–d]. In 2022, Zhu *et al.* reported that the PCE of devices[9] based on oligomers as donor materials was 8.78%, while the V_{oc} was 0.88 V, and J_{sc} was 15.23 mA cm^{-2}.

The conversion efficiency of the binary OSC based on the oligomer as an acceptor is more than 13%, as has been reported.[10] The PCE of the ternary organic solar cells including oligomers can be 17.5% after the green solvent treatment.[11] These researchers have proved that oligomers prolong the molecular conjugation and result in the active layer having better compatibility and film-forming properties of the acceptor material, which is conducive to the formation of the interpenetrating structure, which can promote exciton dissociation and charge transfer, and effectively improve J_{sc} and PCE of the devices.[12]

It is emphasized that the crystallinity of the blend film is an important factor affecting the conversion efficiency.[13] Orderly assembled films with high crystallinity are conducive to the formation of interpenetrating networks between the donors and acceptors, facilitating exciton dissociation and charge transfer, and reducing the energy loss caused by carrier recombination.[14] Reasonable design and optimization of molecules is an effective way to accelerate the development of new photoelectric materials.[15] It is found that effective intramolecular charge transfer (ICT) has a significant effect on the photovoltaic performance of materials.[16] Common donor materials are composed of an electron-donating unit (D), the electron-withdrawing unit (A), and π-bridge, which can be designed as molecules with a push–pull structure. The planarity of the molecular skeleton can be achieved through the regulation of D, A, and π-bridge to help the ICT process.[17] There are a variety of donor and acceptor units that can be used to construct the molecular structure of the push–pull conjugation system.[18] For example, diketopyrrolopyrrole (DPP) is an electron-withdrawing unit widely used in organic optoelectronic materials. The PCE of the polymer (PBDTT–DPP) based on DPP and alkyl thiophene substituted benzodithiophene (BDTT) as the structural unit is 9.66%.[18a] Generally, DPP-based materials show a wide absorption range, even reaching the near-infrared region. Derya Baran's team reported that a DPP-based material covered an absorption range of 300 to 1000 nm.[18e] Two fused electron-deficient lactams form a DPP with great rigidity, which not only improves the utilization of photons but also causes a redshift in absorption. In addition, isooctane can be introduced into the 2,5-position of nitrogen in lactam through side-chain engineering to increase the molecular solubility, which helps to form an ideal active layer.[18h] Scheme 2 provides the synthetic routes for the target compounds **Flu(DPPFlu)$_2$**, **BPF(DPPBPF)$_2$**, **BPF(DPPCz)$_2$**, and **Cz(DPPCz)$_2$**. The introduction of thiophene with weak electron-donating properties on both sides of the lactam not only ensures a strong ICT effect but also makes the whole fragment form a perfect π-conjugate system, providing convenience for carrier transport.[8,12c] The structural diversity of donor materials cannot be separated from the effective electron-donating (D) units. Fluorene (Flu) is a common D component unit. The two benzene rings are connected by a central five-membered ring with excellent planarity, which is conducive to both the intramolecular charge transfer and the formation of effective π–π stacking between molecules in the active layer, which is more conducive to the promotion of carrier transport.[19] In addition, the carbon on the fused ring bridge with sp^3 hybrid (sp^3-C) is replaced by an alkyl chain, which increases the solubility while being orthogonal to the conjugated main chain, to avoid excessive molecular self-aggregation and obtaining ideal active layer morphology.[19d] Furthermore, more surprising is that due to the weak electron-donating ability of Flu, the HOMO energy level is reduced, and the open-circuit (V_{oc}) of Flu-based devices is up to 1.4 V.[20]

In this study, a series of novel oligomer-like donor materials were synthesized, and the photoelectric properties of the new materials were carefully studied through theoretical calculations and experiments. The design concept of the material and the chemical structure of the target molecule are shown in Scheme 1. Based on the previously reported small molecule DPP(Flu)$_2$,[21] the oligomer-like molecule **Flu(DPPFlu)$_2$** was designed and synthesized through structural regulation. Compared with the small molecule DPP (Flu)$_2$, the PCE of the oligomer-like molecule **Flu(DPPFlu)$_2$** was improved. Then, alkoxyphenyl was introduced into **Flu(DPPFlu)$_2$** through the terminal group and side chain regulation to obtain a new oligomer-like molecule **BPF(DPPBPF)$_2$**, which reduced the HOMO level and expanded molecular conjugation, resulting in increased V_{oc} of the device. Next, another new compound **BPF(DPPCz)$_2$** was successfully synthesized by introducing a rigid carbazole terminal unit with stronger electron-donating ability. As an excellent D-unit, carbazole not only ensures the planarity of the molecule but also promotes the ICT process, thus improving the J_{sc} of the device. Finally, an oligomer-like donor material **Cz(DPPCz)$_2$** based on carbazole as both the central core and the terminal unit was synthesized. The PCE of the device using $PC_{71}BM$ as the acceptor reached 6.12%, which is three times higher than the 1.48% that was previously reported for the small molecule DPP(Cz)$_2$.[21b] The relationship between the structure regulation and the charge conduction mechanism is discussed in detail. The ground-state optimized structure and intrinsic optical properties of the material were predicted using the density functional theory (DFT) and time-dependent DFT (TD-DFT) calculations. The photophysical and electrochemical properties of these materials were studied according to absorption spectra and electrochemical cyclic voltammetry curves. BHJ-OSCs with $PC_{71}BM$ as the acceptor were prepared and the relationship between their photovoltaic performance and the structure of the material was studied.

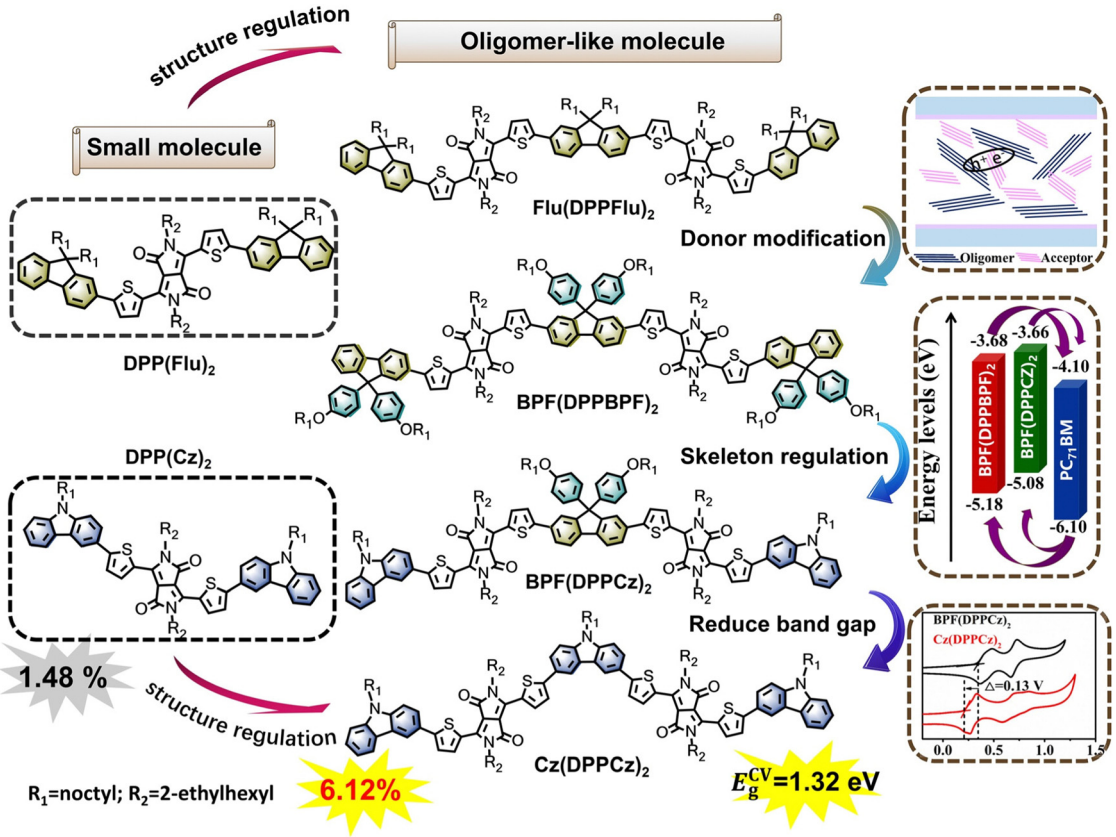

Scheme 1 Molecular design ideas and chemical structures of oligomer-like molecules **Flu(DPPFlu)$_2$**, **BPF(DPPBPF)$_2$**, **BPF(DPPCz)$_2$**, and **Cz(DPPCz)$_2$**.

Experiments and methods

Reagents and materials

Tetrahydrofuran (THF) and toluene (Tol) were treated with standard anhydrous and oxygen-free treatment before use. The materials were synthesized using the standard Schlenk method under N_2 atmosphere. Unless otherwise specified, other reagents and materials were used directly without further purification.

Measurements and instruments

Ultraviolet-visible (UV-Vis) absorption spectra of the oligomer-like materials in the chloroform solution and thin film states were obtained using an Agilent Cary 5000 spectrophotometer. Cyclic voltammetry (CV) curves were measured using the CHI610D electrochemical workstation from CH Instruments, and the measurements were performed in 0.1 M anhydrous Bu_4NBF_4/CH_2Cl_2 solution under N_2 atmosphere at a scan rate of 100 mV s^{-1} with a glass-carbon electrode, Ag/Ag^+ electrode (Ag in 0.1 M $AgNO_3$ solution of acetonitrile), and platinum wire electrode as the working electrode, reference electrode, and counter electrode, respectively, and the ferrocene-ferrocenium (Fc/Fc^+) couple as the internal standard. Thermogravimetric analysis (TGA) was measured on a TA Instruments Q50 thermogravimetric analyzer under N_2 atmosphere with a heating rate of 10 °C min^{-1}. The current–voltage (*J–V*) characteristics of OSCs were tested on a computer-controlled Keithley 2400 Source Measure Unit under AM 1.5 G illumination at an intensity of 100 mW cm^{-2}. The (*J–V*) characteristics of the hole-only and electron-only OSCs were also tasted in the same way in the dark. The external quantum efficiency (EQE) spectra of OSCs were obtained using an integrated system IQE 200 (Newport, America) in a monochromatic light from a 75 W Xenon lamp, and a calibrated silicon photodiode was used to determine the light intensity. The contact angle measurement was performed using the contact angle system (JC2000D1, Powereach, China).

Synthesis and characterization

The synthetic routes for all oligomer molecules are shown in Scheme 2. Compounds **1** and **D1–D6** were synthesized according to the procedures reported in the literature.[19c,22] Firstly, compounds **2–4** were synthesized by the $Pd(PPh_3)_2Cl_2$ catalyzed Suzuki coupling reaction.[22c] Subsequently, compounds **2–4** were converted to intermediate compounds **5–7** through the *N*-bromosuccinimide(NBS) bromination reaction.[22d] Finally, the four donor materials **Flu(DPPFlu)$_2$**, **BPF(DPPBPF)$_2$**, **BPF(DPPCz)$_2$**, and **Cz(DPPCz)$_2$** were obtained by the $Pd(PPh_3)_2Cl_2$ catalyzed Suzuki coupling reaction. The chemical structures of the new compounds were confirmed by ^1H NMR and ^{13}C NMR spectroscopy (a Bruker AVANCE II 400/500 MHz and 100 MHz spectrometer, respectively), and high-resolution mass spectrometry (HRMS) (MALDIMicro MX spectrometer).

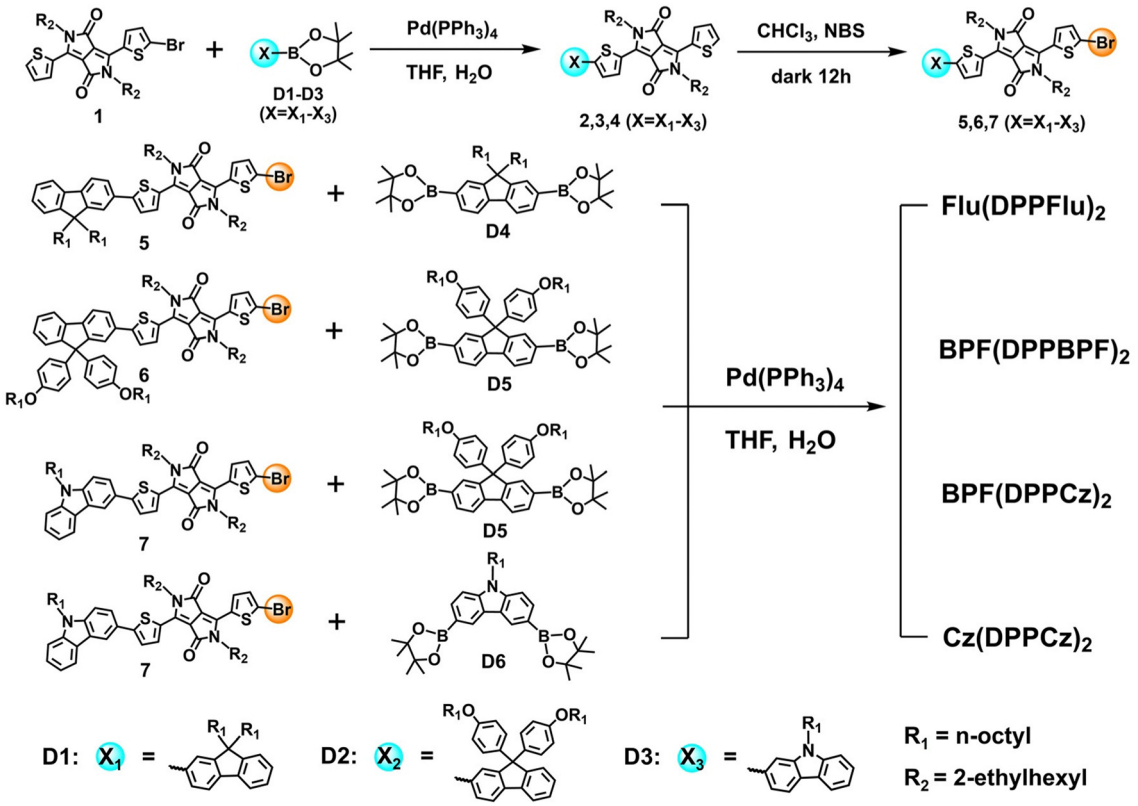

Scheme 2 Synthetic routes for the target compounds **Flu(DPPFlu)$_2$**, **BPF(DPPBPF)$_2$**, **BPF(DPPCz)$_2$** and **Cz(DPPCz)$_2$**.

Synthesis of compound 2

A mixture of compound **1** (362 mg, 0.6 mmol), compound **D1** (322 mg, 0.62 mmol), $Pd(PPh_3)_2Cl_2$ (13 mg, 0.01 mmol), K_2CO_3 (3.04 g, 22 mmol), THF (30 mL), and H_2O (11 mL) was heated at 80 °C for 24 h under N_2 atmosphere. After cooling to room temperature, the reaction solution was poured into 30 mL of water and extracted with chloroform (20 mL × 3). The organic layer was collected and dried with anhydrous Na_2SO_4. After evaporating the organic solvent under reduced pressure, the residue was purified using a silica gel chromatographic column with petroleum ether/CH_2Cl_2 (1 : 1 v/v) to afford a purple solid (366 mg, 70%). M.p.: 95–97 °C. ^{1}H NMR (500 MHz, $CDCl_3$, ppm):δ 9.01 (s, 1H), 8.88 (s, 1H), 7.72 (t, J = 6.3 Hz, 2H), 7.67 (d, J = 7.8 Hz, 1H), 7.61 (s, 2H), 7.53 (d, J = 4.1 Hz, 1H), 7.36–7.33 (m, 3H), 7.28 (d, J = 4.3 Hz, 1H), 4.10 (t, J = 8.6 Hz, 2H), 4.06 (t, J = 7.3 Hz, 2H), 2.02–1.99 (m, 4H), 1.90–1.86 (m, 1H), 1.44–1.35 (m, 9H), 1.36–1.30 (m, 6H), 1.26–1.24 (m, 2H), 1.20–1.16 (m, 4H), 1.10–1.06 (m, 16H), 0.95–0.92 (m, 3H), 0.88 (m, 9H), 0.81 (t, J = 7.5 Hz, 6H), 0.68–0.64 (m, 4H).

Synthesis of compound 3

A mixture of compound **1** (604 mg, 1 mmol), compound **D2** (700.1 mg, 1 mmol), $Pd(PPh_3)_2Cl_2$ (14 mg, 0.01 mmol), K_2CO_3 (2.7 g, 20 mmol), THF (30 mL), and H_2O (11 mL) was heated at 80 °C for 24 h under N_2 atmosphere. After cooling to room temperature, the reaction solution was poured into 30 mL of water and extracted with chloroform (20 mL × 3). The organic layer was collected and dried with anhydrous Na_2SO_4. After evaporating the organic solvent under reduced pressure, the residue was purified using the silica gel chromatographic column with petroleum ether/CH_2Cl_2 (1 : 1 v/v) to afford the purple solid (886 mg, 80%). M.p.: 81–83 °C. ^{1}H NMR (500 MHz, $CDCl_3$, ppm) δ 8.97–8.86 (m, 2H), 7.77 (t, J = 7.4 Hz, 2H), 7.66 (d, J = 10.1 Hz, 2H), 7.61 (s, 1H), 7.42 (d, J = 4.1 Hz, 1H), 7.39–7.34 (m, 2H), 7.31–7.26 (m, 2H), 7.14 (d, J = 8.5 Hz, 4H), 6.76 (d, J = 8.6 Hz, 4H), 4.06–3.99 (m, 4H), 3.89 (t, J = 6.5 Hz, 4H), 1.93–1.85 (m, 2H), 1.76–1.70 (m, 4H), 1.54 (m, 2H), 1.43–1.35 (m, 10H), 1.34–1.23 (m, 30H), 0.87 (t, J = 6.8 Hz, 12H).

Synthesis of compound 4

A mixture of compound **1** (262 mg, 0.6 mmol), compound **D3** (248.5 mg, 0.6 mmol), $Pd(PPh_3)_2Cl_2$ (14 mg, 0.01 mmol), K_2CO_3 (2.7 g, 20 mmol), and THF (30 mL) and H_2O (11 mL) was heated at 80 °C for 24 h under N_2 atmosphere. After cooling to room temperature, the reaction solution was poured into 30 mL of water and extracted with chloroform (20 mL × 3). The organic layer was collected and dried with anhydrous Na_2SO_4. After evaporating the organic solvent under reduced pressure, the residue was purified using a silica gel chromatographic column with petroleum ether/CH_2Cl_2 (1 : 1 v/v) to afford purple solid (373 mg, 76%). M.p.: 138–139 °C. ^{1}H NMR (500 MHz, $CDCl_3$, ppm) δ 9.06 (d, J = 4.0 Hz, 1H), 8.86 (d, J = 3.4 Hz, 1H), 8.38 (d, J = 1.4 Hz, 1H) 8.15 (d, J = 7.7 Hz, 1H), 7.79 (dd, J = 8.5, 1.7 Hz, 1H), 7.60 (d, J = 4.7 Hz, 1H), 7.53–7.50 (m, 2H), 7.43

(d, J = 8.4 Hz, 2H), 7.28 (dd, J = 8.5, 6.1 Hz, 2H), 4.31 (t, J = 7.2 Hz, 2H), 4.13–4.03 (m, 4H), 2.02–1.96 (m, 1H), 1.91–1.86 (m, 3H), 1.40–1.24 (m, 26H), 0.95 (t, J = 7.5 Hz, 3H), 0.91–0.85 (m, 12H).

Synthesis of compound 5

Solution of NBS (76 mg, 0.4 mmol) in chloroform (5 mL) was added dropwise to the solution of compound **2** (360 mg, 0.4 mmol) in chloroform (10 mL) and the mixture was stirred continuously for 12 h at room temperature. The resulting solution was poured into 30 mL of water and extracted with chloroform (20 mL × 3). The organic layer was collected and dried with anhydrous Na_2SO_4. After evaporating the organic solvent under reduced pressure, the residue was purified using a silica gel chromatographic column with petroleum ether/CH_2Cl_2 (1 : 1 v/v), afford purple solid (390 mg, 78%). M.p.: 109–111 °C. ^{1}H NMR (500 MHz, $CDCl_3$, ppm) δ 9.02 (d, J = 3.0 Hz, 1H), 8.62 (s, 1H), 7.72 (dd, J = 9.0, 4.8 Hz, 2H), 7.67 (d, J = 8.0 Hz, 1H), 7.61 (s, 1H), 7.53 (d, J = 4.1 Hz, 1H), 7.37–7.31 (m, 3H), 7.26 (s, 1H), 4.15–4.04 (m, 2H), 4.02–3.92 (m, 2H), 2.00 (t, J =7.5 Hz, 4H), 1.90–1.82 (m, 1H), 1.42–1.25 (m, 17H), 1.21–1.15 (m, 4H), 1.11–1.03 (m, 16H), 0.94 (t, J = 7.5 Hz, 3H), 0.87 (t, J = 7.5 Hz 9H), 0.80 (t, J = 7.2 Hz, 6H), 0.66–0.64 (m, 4H).

Synthesis of compound 6

Solution of NBS (80 mg, 0.4 mmol) in chloroform (10 mL) was added dropwise to the solution of compound **3** (440 mg, 0.4 mmol) in chloroform (15 mL) and the mixture was stirred continuously for 12 h at room temperature. The resulting solution was poured into 30 mL of water and extracted with chloroform (20 mL × 3). The organic layer was collected and dried with anhydrous Na_2SO_4. After evaporating the organic solvent under reduced pressure, the residue was purified using a silica gel chromatographic column with petroleum ether/CH_2Cl_2 (2 : 1 v/v), afford purple solid (239 mg, 75%). M.p.: 115–116 °C. ^{1}H NMR (500 MHz, $CDCl_3$, ppm) δ 8.97 (s, 1H), 8.60 (s, 1H), 7.77 (t, J = 7.2 Hz, 2H), 7.66 (d, J = 8.4 Hz, 2H), 7.41 (d, J = 4.1 Hz, 1H), 7.37 (dd, J = 10.0, 5.0 Hz, 2H), 7.29 (t, J = 7.4 Hz, 1H), 7.21 (d, J = 4.1 Hz, 1H), 7.13 (d, J = 8.8 Hz, 4H), 6.76 (d, J = 8.8 Hz, 4H), 4.06–4.01 (m, 2H), 3.95 (m, 2H), 3.89 (m, 4H), 1.92–1.87 (m, 1H), 1.86–1.82 (m, 1H), 1.76–1.70 (m, 4H), 1.43–1.35 (m, 10H), 1.33–1.24 (m, 26H), 0.91 (t, J = 7.5 Hz, 6H), 0.86 (t, J = 6.8 Hz, 9H), 0.82 (t, J = 7.0 Hz, 3H).

Synthesis of compound 7

A solution of NBS (126 mg, 0.7 mmol) in chloroform (10 mL) was added dropwise to a solution of compound **4** (520 mg, 0.6 mmol) in chloroform (15 mL), and the mixture was stirred continuously for 12 h at room temperature. The resulting solution was poured into 30 mL of water and extracted with chloroform (20 mL × 3). The organic layer was collected and dried with anhydrous Na_2SO_4. After evaporating the organic solvent under reduced pressure, the residue was purified using a silica gel chromatographic column with petroleum ether/CH_2Cl_2 (1 : 1 v/v), affording a purple solid (466 mg, 82%). M.p.: 157–158 °C. ^{1}H NMR (500 MHz, $CDCl_3$, ppm) δ 9.07 (d, J = 4.1 Hz, 1H), 8.59 (d, J = 4.1 Hz, 1H), 8.38 (d, J = 1.9 Hz, 1H), 8.15 (d, J = 7.8 Hz, 1H), 7.78 (dd, J = 8.5, 1.9 Hz, 1H), 7.51 (dd, J = 9.3, 4.8 Hz, 2H), 7.42 (d, J = 8.5 Hz, 2H), 7.29 (d, J = 7.4 Hz, 1H), 7.21 (d, J = 4.1 Hz, 1H), 4.31 (t, J = 7.3 Hz, 2H), 4.15–4.05 (m, 2H), 4.02–3.91 (m, 2H), 2.05–1.95 (m, 1H), 1.92–1.82 (m, 3H), 1.42–1.24 (m, 26H), 0.94 (t, J = 7.5 Hz, 3H), 0.91–0.85 (m, 12H).

Synthesis of Flu(DPPFlu)$_2$

A mixture of compound **5** (322 mg, 0.32 mmol), **D4** (99 mg, 0.15 mmol), $Pd(PPh_3)_2Cl_2$ (13 mg, 0.01 mmol), K_2CO_3 (414 mg, 3 mmol), THF (30 mL) and H_2O (4 mL) was heated at 80 °C for 48 h under N_2 atmosphere. After cooling to room temperature, the reaction solution was poured into 30 mL of water and extracted with chloroform (30 mL × 3). The organic layer was collected and dried over Na_2SO_4. After evaporating the organic solvent under reduced pressure, the residue was purified by silica gel chromatographic column with petroleum ether/CH_2Cl_2 (1 : 5 v/v) as the eluent to afford **Flu(DPPFlu)$_2$** as a navy blue solid (258 mg, 77%). M.p.: 95–97 °C. ^{1}H NMR (500 MHz, $CDCl_3$, ppm): δ 9.01 (s, 2H), 7.77–7.71 (m, 8H), 7.68 (d, J = 7.9 Hz, 2H), 7.63 (d, J = 8.7 Hz, 4H), 7.55 (dd, J = 8.4, 4.0 Hz, 4H), 7.35 (d, J = 5.9 Hz, 8H), 4.19–4.09 (m, 10H), 2.09–2.05 (m, 4H), 2.04–1.98 (m, 14H), 1.65 (t, J = 13.5 Hz, 2H), 1.56 (s, 4H), 1.45–1.40 (m, 14H), 1.32 (d, J = 3.2 Hz, 10H), 1.20–1.17 (m, 10H), 1.11–1.06 (m, 44H), 0.96 (t, J = 5.0 Hz,12H), 0.90 (t, J = 5.0 Hz, 12H), 0.80 (t, J = 7.2 Hz, 18H), 0.75–0.62 (m, 16H). ^{13}C NMR (126 MHz, $CDCl_3$, ppm) 160.83, 160.78, 151.22, 150.85, 150.09, 149.71, 149.19, 141.21, 140.23, 139.27, 138.91, 138.59, 135.95, 135.77, 131.51, 130.91, 127.77, 127.47, 126.60, 125.96, 124.43, 124.21, 123.43, 123.24, 121.97, 119.63, 119.27, 118.98, 107.39, 107.24, 54.52, 54.27, 45.03, 39.30, 38.37, 34.43, 31.70, 30.87, 30.74, 30.60, 29.51, 28.98, 28.69, 28.17, 27.92, 27.61, 25.92, 25.43, 25.33, 22.84, 22.80, 22.46, 22.36, 22.26, 22.13, 21.86, 21.67, 21.56, 21.41, 13.06, 13.00, 9.68.HRMS (MALDI-TOF): 2211.4247, [M^+] (calcd for $C_{147}H_{198}N_4O_4S_4$:2211.4296).

Synthesis of BPF(DPPBPF)$_2$

A mixture of compound **6** (245 mg, 0.2 mmol), **D5** (75 mg, 0.1 mmol), $Pd(PPh_3)_2Cl_2$ (13 mg, 0.01 mmol), K_2CO_3 (250mg, 1.8mmol), THF (30 mL) and H_2O (4 mL) was heated at 80 °C for 48 h under N_2 atmosphere. After cooling to room temperature, the reaction solution was poured into 30 mL of water and extracted with chloroform (30 mL × 3). The organic layer was collected and dried over Na_2SO_4. After evaporating the organic solvent under reduced pressure, the residue was purified by silica gel chromatographic column with petroleum ether/CH_2Cl_2 (1 : 3 v/v) as the eluent to afford **BPF(DPPBPF)$_2$** as a navy blue solid(170 mg, 69%). M.p.: 143–145 °C. ^{1}H NMR (500 MHz, $CDCl_3$, ppm) δ 8.93 (d, J = 1.5 Hz, 2H), 7.78–7.71 (m, 8H), 7.66 (d, J = 9.8 Hz, 4H), 7.55 (s, 2H), 7.42 (d, J = 3.9 Hz, 4H), 7.37 (d, J = 7.9 Hz, 4H), 7.18 (d, J = 8.9 Hz, 2H), 7.14 (d, J = 8.8 Hz, 8H), 7.10 (d, J = 3.8 Hz, 2H), 6.80–6.74 (m, 16H), 4.06 (s, 4H), 3.89 (t, J = 6.3 Hz, 12H), 3.36 (s, 4H), 3.30–3.18 (m, 2H), 3.06–2.91 (m, 2H), 1.96–1.87 (m, 4H), 1.75–1.71 (m, 16H), 1.43–1.37 (m, 20H), 1.33 (s, 16H), 1.29–1.24 (m, 48H), 0.91 (t, J = 7.4 Hz, 12H), 0.86

(t, J = 5.1 Hz, 18H), 0.82 (t, J = 7.5 Hz, 12H). ^{13}C NMR (126 MHz, $CDCl_3$, ppm) δ 181.69, 165.87, 162.73, 162.36, 158.94, 158.32, 158.27, 158.22, 158.12, 158.07, 158.03, 153.06, 152.90, 152.46, 152.35, 146.76, 141.41, 141.14, 140.29, 139.98, 139.91, 139.31, 139.19, 139.05, 137.56, 137.45, 137.36, 137.28, 136.92, 136.85, 136.77, 135.51, 133.25, 132.87, 132.78, 132.54, 129.12, 128.32, 127.90, 127.47, 127.41, 126.10, 125.98, 124.26, 123.40, 120.75, 120.47, 120.20, 114.45, 114.40, 114.26, 114.21, 67.97, 64.47, 64.36, 51.20, 45.98, 41.98, 39.26, 38.89, 38.11, 31.82, 30.93, 30.76, 30.71, 30.38, 29.36, 29.32, 29.23, 28.68, 28.62, 28.50, 26.09, 24.37, 24.11, 23.98, 23.79, 23.09, 23.00, 22.93, 22.65, 22.51, 14.08, 14.02, 13.96, 10.89, 10.79, 10.68, 10.58, 10.46, 10.39, 10.19. HRMS(MALDI-TOF): 2763.5967, [M^+] (calcd for $C_{147}H_{198}N_4O_4S_4$:2763.5869).

Synthesis of BPF(DPPCz)$_2$

A mixture of compound **7** (296 mg, 0.16 mmol), **D5** (132 mg, 0.3 mmol), $Pd(PPh_3)_2Cl_2$ (13 mg, 0.01 mmol), K_2CO_3 (441 mg, 3.2 mmol), THF (30 mL) and H_2O (2 mL) was heated at 80 °C for 48 h under N_2 atmosphere. After cooling to room temperature, the reaction solution was poured into 30 mL of water and extracted with chloroform (30 mL × 3). The organic layer was collected and dried over Na_2SO_4. After evaporating the organic solvent under reduced pressure, the residue was purified using the silica gel chromatographic column with petroleum ether/CH_2Cl_2 (1 : 4 v/v) as the eluent to afford **BPF(DPPCz)$_2$** as a navy blue solid (287 mg, 82%). M.p.: 218–220 °C. ^{1}H NMR (500 MHz, $CDCl_3$, ppm) δ 9.05 (s, 2H), 8.94 (s, 2H), 8.36 (s, 2H), 8.14 (d, J = 7.6 Hz, 2H), 7.76 (d, J = 5.4 Hz, 4H), 7.65 (s, 4H), 7.49 (t, J = 7.5 Hz, 4H), 7.40 (d, J = 8.0 Hz, 6H), 7.28 (d, J = 7.3 Hz, 2H), 7.20 (d, J = 8.5 Hz, 4H), 6.81 (d, J = 8.4 Hz, 4H), 4.29 (s, 4H), 4.08 (d, J = 22.1 Hz, 8H), 3.91 (t, J = 6.3 Hz, 4H), 2.01 (s, 2H), 1.96–1.83 (m, 8H), 1.77–1.73 (m, 4H), 1.44–1.36 (m, 30H), 1.32–1.26 (m, 40H), 0.94 (t, J = 5.0 Hz, 6H), 0.90 (t, J = 11.8, 5.0 Hz, 12H), 0.85 (t, J = 5.0 Hz, 18H). ^{13}C NMR (126 MHz, $CDCl_3$, ppm) δ 161.75, 158.34, 153.37, 140.94, 140.77, 140.30, 139.80, 137.62, 136.99, 133.15, 129.36, 129.16, 127.68, 126.46, 126.26, 124.14, 123.45, 123.33, 122.72, 121.06, 120.99, 120.90, 120.60, 119.99, 119.45, 118.17, 118.06, 117.91, 114.46, 109.11, 68.03, 64.48, 46.05, 45.94, 43.18, 39.31, 31.82, 31.80, 31.35, 30.51, 30.41, 29.37, 29.25, 29.18, 29.03, 28.68, 28.56, 28.25, 27.41, 27.30, 26.24, 26.11, 23.82, 23.20, 23.13, 22.66, 22.61, 14.14, 14.07, 10.97, 10.71, 10.69. HRMS (MALDI-TOF): 2173.2266, [M^+] (calcd for $C_{147}H_{198}N_4O_4S_4$:2173.2221).

Synthesis of Cz(DPPCz)$_2$

A mixture comprising compound **7** (302 mg, 0.2 mmol), **D6** (66 mg, 0.1 mmol), $Pd(PPh_3)_2Cl_2$ (13 mg, 0.01 mmol), K_2CO_3 (342 mg, 2 mmol), THF (30 mL) and H_2O (2 mL) was heated at 80 °C for 48 h under the N_2 atmosphere. After cooling to room temperature, the reaction solution was poured into 30 mL water and extracted with chloroform (30 mL × 3). The organic layer was collected and dried over Na_2SO_4. After evaporating the organic solvent under reduced pressure, the residue was purified using the silica gel chromatographic column with petroleum ether/CH_2Cl_2 (1 : 5 v/v) as the eluent to afford **BPF(DPPCz)$_2$** as a navy blue solid (151 mg, 65%). M.p.: 187–189 °C. ^{1}H NMR (500 MHz, $CDCl_3$, ppm) δ 9.06 (d, J = 5.0 Hz, 2H), 9.02 (d, J = 5.0 Hz, 2H), 8.33 (d, J = 10.0 Hz, 4H), 8.13 (d, J = 7.7 Hz, 2H), 7.75 (t, J = 8.2 Hz, 4H), 7.52–7.46 (m, 6H), 7.40–7.35 (m, 6H), 7.28 (d, J = 7.4 Hz, 2H), 4.24 (t, J = 7.0 Hz, 6H), 4.16–4.06 (m, 8H), 2.01 (d, J = 5.3 Hz, 4H), 1.90–1.82 (m, 6H), 1.47–1.43 (m, 20H), 1.37–1.33 (m, 22H), 1.29–1.24 (m, 20H), 0.96 (t, J = 7.3 Hz, 12H), 0.91 (t, J = 6.6 Hz, 12H), 0.86 (t, J = 6.9 Hz, 9H). ^{13}C NMR (126 MHz, $CDCl_3$, ppm) δ 161.68, 161.62, 151.31, 150.58, 141.03, 140.95, 140.65, 139.62, 139.19, 137.21, 136.87, 127.98, 127.63, 126.20, 124.99, 124.66, 124.31, 124.06, 123.41, 123.29, 123.08, 122.72, 120.59, 119.36, 117.88, 109.48, 109.12, 109.02, 107.86, 107.66, 46.05, 43.34, 43.17, 39.37, 31.78, 30.54, 29.34, 29.16, 29.00, 28.95, 28.72, 27.28, 26.93, 23.90, 23.85, 23.34, 23.21, 22.73, 22.59, 14.19, 14.14, 14.04, 10.74, 10.72. HRMS (MALDI-TOF): 1878.0334, [M^+] (calcd for $C_{147}H_{198}N_4O_4S_4$:1878.0397).

Thermal stability

To determine the thermal stability of the four materials, thermogravimetric analysis (TGA) was carried out for the four materials, and the curves are shown in Fig. 1. All four new materials showed 5% weight loss at decomposition temperatures (T_d) of above 400 °C. The T_d of **Flu(DPPFlu)$_2$**, **BPF(DPPBPF)$_2$**, **BPF(DPPCz)$_2$** and **Cz(DPPCz)$_2$** were 418 °C and 420 °C, 424 °C, and 408 °C, respectively. Therefore, the four compounds showed excellent thermal stability, fully meeting the basic requirements of OSC materials for the device preparation.

Theoretical calculations

Theoretical calculation and simulation are recognized as a convenient and effective method to verify the rationality of new material design.[23] According to DFT and TD-DFT, using B3LYP/6-31G (d) as the basis set, the electronic density distribution, frontier molecular orbital (FMO) energy level, absorption spectrum, density of state (DOS), and electrostatic

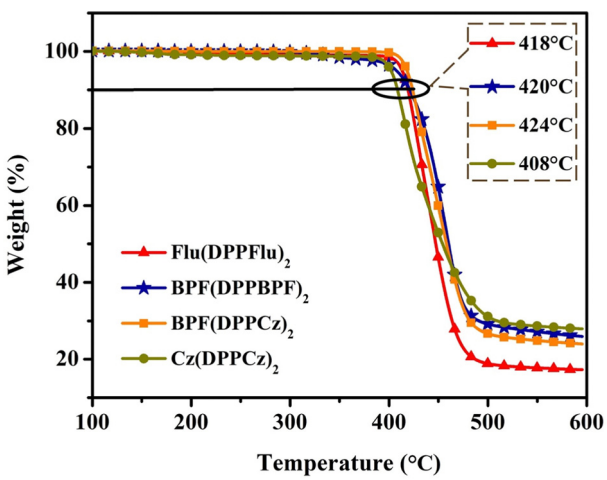

Fig. 1 TGA curves of compounds **Flu(DPPFlu)$_2$**, **BPF(DPPBPF)$_2$**, **BPF(DPPCz)$_2$**, and **Cz(DPPCz)$_2$** at a heating rate of 10 °C min^{-1} under nitrogen flow.

potential (ESP) can be calculated and simulated theoretically.[24] It should be noted that in order to simplify the calculation process, the long alkyl chains R_1 and R_2 are replaced by methyl groups. The optimized geometries with torsion angles, calculated molecular orbital energy levels, and predicted UV-Vis absorption spectra are shown in Fig. 2. The calculated data are listed in Table 1, and more TD-DFT calculation results are summarized in Table S2 (in ESI†). From the overall perspective, **Flu(DPPFlu)$_2$** and **BPF(DPPBPF)$_2$** are linear, and the torsion angle of the terminal group is approximately 23°, as shown in Fig. 2(a). This structure should be conducive to intermolecular π–π stacking and carrier transport.[24d] With the introduction of carbazole units, the molecular skeletons of **BPF(DPPCz)$_2$** and **Cz(DPPCz)$_2$** are bent, and oligomer-like molecule **Cz(DPPCz)$_2$** is V-shaped. The torsion angle of the terminal carbazole groups of the two molecules increased slightly to about 26°. It is hoped to promote the intramolecular ICT and increase the J_{sc} through the introduction of a carbazole group with relatively strong electron-donating ability. As shown in Fig. 2(b), the changes in the electron density distribution of the four molecules illustrate the intramolecular charge transfer. Especially for oligomer-like molecule **Cz(DPPCz)$_2$**, due to the presence of the carbazole unit with strong electron-donating ability; the electron cloud of LUMO level is mainly concentrated on the DPP unit with strong electron-withdrawing ability, which is a good indicator of charge transfer. The oligomer-like molecule **BPF(DPPBPF)$_2$** was obtained by introducing alkoxyphenyl to the terminal group of **Flu(DPPFlu)$_2$**. The structural design of the weak electron-donating group reduces the HOMO energy level from −4.70 to −4.76 eV, which is beneficial to the improvement of the V_{oc}. The introduction of the terminal carbazole groups in **BPF(DPPCz)$_2$** molecule increases the HOMO energy level to 4.58 eV, and the decrease in the band gap helps to improve J_{sc}. Finally, the band gap of the oligomer-like molecule **Cz(DPPCz)$_2$** was further reduced to 2.07 eV, due to the relatively strong electron-donating ability of the carbazole group, which promoted the ICT process and contributed to the improvement of J_{sc}. The predicted absorption spectra calculated using TD-DFT are shown in Fig. 2(c). All molecules show two distinct absorption peaks covering the absorption range of 300–1100 nm, indicating excellent optical absorption properties. The strong absorption peaks of all molecules in the low-energy region are 640, 670, 672, and 687 nm, respectively, due to the transition from HOMO to LUMO energy levels. While the absorption peaks in the high-energy region are attributed to the transition from HOMO−2 to LUMO of **Flu(DPPFlu)$_2$** at 428 nm, the transition from HOMO−6 to LUMO of **BPF(DPPBPF)$_2$** at 431 nm, the transition from HOMO−4 to LUMO+1 of **BPF(DPPCz)$_2$** at 440 nm, and the transition from HOMO−3 to LUMO+1 of **Cz(DPPCz)$_2$** at 450 nm. The gradual red shift in the absorption wavelength demonstrates the gradual improvement of the material's absorption ability to sunlight, which indirectly suggests that the molecular photovoltaic performance is gradually optimized. The above research first theoretically demonstrates the rationality of molecular structure design, and the material structure determines their properties.

To better understand the charge conduction and electron excitation at the molecular level, it is necessary and reliable to analyze the density of states (DOS), including the total density of states (TDOS), partial density of states (PDOS), and overlap density of states (OPDOS).[24e] TDOS is the sum of the relative strengths of the entire molecule, while PDOS divides the molecule into specific segments to better understand the relative strengths contributed by different segments. In addition, OPDOS corresponds to the overlap density of the states between fragments 1 and 2 in each molecule. When its relative

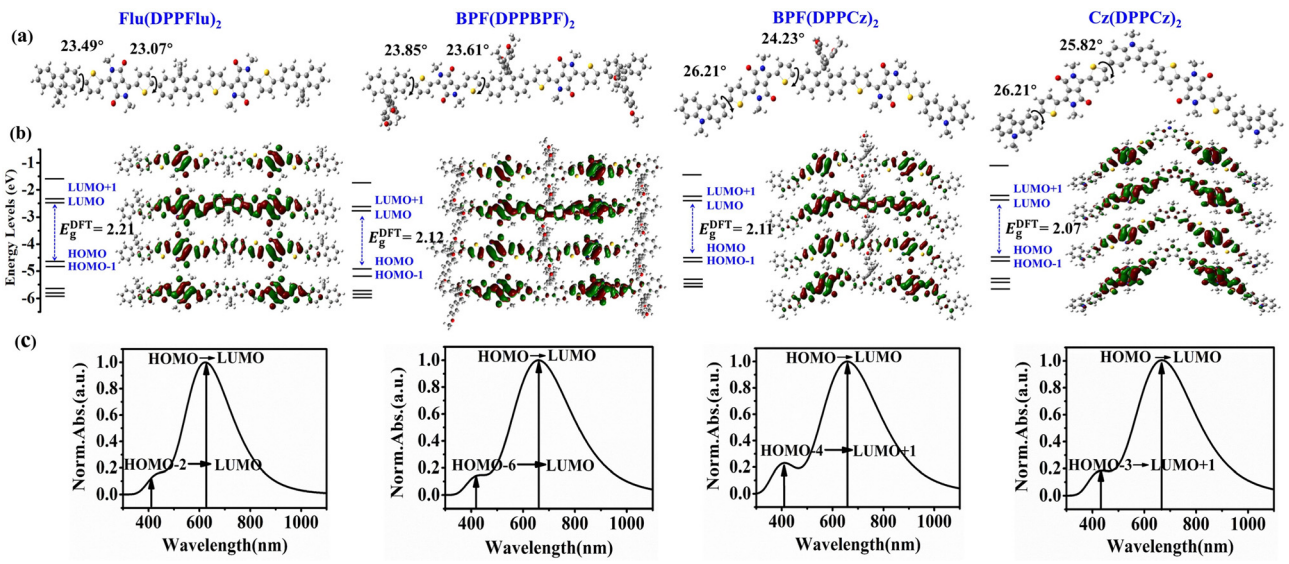

Fig. 2 Summary of the theoretical calculations with DFT/TD-DFT methods for **Flu(DPPFlu)$_2$**, **BPF(DPPBPF)$_2$**, **BPF(DPPCz)$_2$**, and **Cz(DPPCz)$_2$**; (a) optimized geometries with torsion angles; (b) calculated molecular orbital energy levels and electronic cloud distributions; and (c) predicted UV-Vis absorption spectra.

Table 1 The photophysical, electrochemical and theoretical calculated data of **Flu(DPPFlu)$_2$**, **BPF(DPPBPF)$_2$**, **BPF(DPPCz)$_2$**, and **Cz(DPPCz)$_2$**

Compound	UV-Vis absorption				Cyclic voltammetry			DFT calculations			
	λ_{max}^{sol} (nm)/ε (10^5 M^{-1} cm^{-1})	λ_{max}^{film} (nm)	E_g^{opt} (eV)	HOMO^{CV}/LUMO^{CV} (eV)	E_g^{CV} (eV)	HOMO^{DFT}/LUMO^{DFT} (eV)	E_g^{DFT} (eV)	D (Å)	$\Delta\sigma$ (Å)	Sr (Å)	E_{coul} (eV)
Flu(DPPFlu)$_2$	644/1.05	660	1.75	−5.10/−3.54	1.56	−4.70/−2.49	2.21	0.31	0.23	0.82	2.14
BPF(DPPBPF)$_2$	647/0.99	658	1.72	−5.18/−3.68	1.50	−4.76/−2.62	2.14	2.99	0.12	0.81	2.09
BPF(DPPCz)$_2$	636/1.09	666	1.66	−5.08/−3.66	1.42	−4.58/−2.47	2.11	0.87	1.14	0.80	2.06
Cz(DPPCz)$_2$	652/1.24	683	1.63	−4.95/−3.63	1.32	−4.53/−2.46	2.07	0.68	0.21	0.82	2.02

strength is positive, it means the bonding orbital, while the negative value is the anti-bonding molecular orbital between the two segments. The DOS curves of the designed molecules obtained with theoretical calculation are shown in Fig. 3. The central line position of the *X*-axis of the DOS curve corresponds to the HOMO energy level. The left and right sides of the curves represent the ground and excited states, respectively. The *Y*-axis corresponds to the relative strength and the ratio of DOS to OPDOS is set to 1 : 1. The four D–A–D–A–D type oligomer-like molecules in this study split the fragments in a similar manner, which are three donor fragments and two acceptor fragments. In the DOS diagram, the upper black line represents the sum of the relative intensities of the density of states (TDOS), and the lower red, blue, pink, grey, and green lines (frag. 1–5) represent the specific contributions of each segment in the molecule from left to right to the total absorption (PDOS). As shown in Fig. 3(a), the contributions of the two electron-withdrawing units (DPP, frag. 2 and frag. 4) of the **Flu(DPPFlu)$_2$** molecule are significantly larger than those of the three electron-donating units (Flu, frag. 1, frag. 3 and frag. 5) in the ground and excited states, demonstrating that the electron-withdrawing units play an important role in charge dispersion. On the contrary, in the **BPF(DPPBPF)$_2$** molecule, as shown in Fig. 3(b), all the contributions arise from a balanced distribution amongst the donor and accept units (frag. 1–5), which may be due to the introduction of the alkoxyphenyl group expanded molecular conjugation. In Fig. 3(c), the contribution of the central position BPF (frag. 3) and DPP (frag. 2 and 4) are particularly prominent, while the relative intensity of the carbazole unit is similar, suggesting that the electron density distribution can be altered as the differences in the electron-withdrawing ability of different fragments in **BPF(DPPCz)$_2$** is caused by the terminal replacement. As shown in Fig. 3(d), the **Cz(DPPCz)$_2$** molecule can be seen from the uniform distribution of peaks in that the intensity of the contributions of all segments is similar. This is because the oligomer-like molecules facilitate more homogeneous charge conduction and improve carrier mobility when electron-donating and electron-withdrawing fragments are highly matched. Inspection of the OPDOS curves suggests that interactions between the electron-donating and electron-withdrawing fragments are important for the stabilization of the four materials. Because of their similar OPDOS relative intensities in the ground states, donor fragments slightly overlap with acceptor fragment, which is still beneficial to bonding. The OPDOS curve is in the negative region in the excited states and shows antibonding characteristics, this is due to the unfavourable overlapping in the orbital phase. The results show that the strong interaction between the donor fragment and the acceptor fragment is beneficial to promote ICT, thereby optimizing the photovoltaic properties of the material.

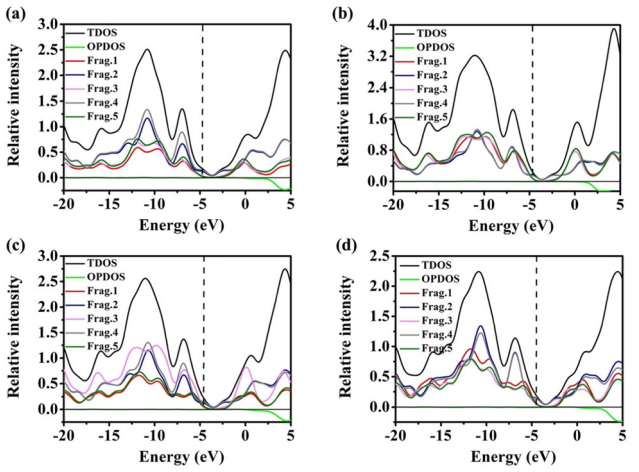

Fig. 3 The DOS curves of the designed molecules obtained with theoretical calculations: (a) **Flu(DPPFlu)$_2$**, (b) **BPF(DPPBPF)$_2$**, (c) **BPF(DPPCz)$_2$**, and (d) **Cz(DPPCz)$_2$**.

To further study the mechanism of intermolecular electric field (IEF), it is necessary not only to study the relative strength of the energy through the DOS but the clarification of the difference between the driving force of the charge transfer through the surface electrostatic potential (ESP) of the donor and acceptor parts[24d] is required. The three-dimensional molecular surface ESP diagrams of the four designed molecules are shown in Fig. 4(a). The electrostatic potential area is distinguishable, and the movement of the electrostatic potential from negative to positive is indicated by the potential bar in colour: red < yellow < green < cyan < blue. It can be clearly distinguished that the red low potential (electrophilic or acceptor) is mainly concentrated on the oxygen atom of the DPP part, while the blue high potential (nucleophilic region or donor) is mainly distributed in the electron-donating part of each molecule. The electrostatic potentials of the four molecules are −4.816 to 4.816 e^{-2} for **Flu(DPPFlu)$_2$**, −5.300 to 5.300 e^{-2} for **BPF(DPPBPF)$_2$**, −5.059 to −5.059 e^{-2} for **BPF(DPPCz)$_2$**, and −5.780 to 5.780 e^{-2} for **Cz(DPPCz)$_2$**, where **Cz(DPPCz)$_2$** shows the highest electron-donating potential. The molecular electrostatic potential revealed the occurrence of the intramolecular interactions and the information on the reactive sides for the

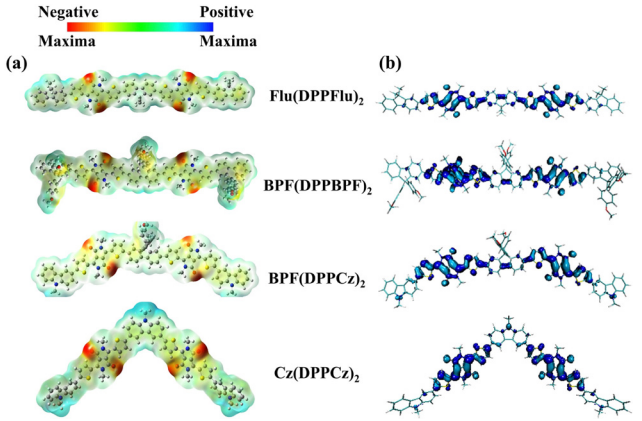

Fig. 4 (a) Three-dimensional molecular surface electrostatic potential (ESP) diagrams for four designed molecules; (b) electron–hole leap mechanisms from the ground state (S_0) to the excited state (S_1).

attack of electrophiles and nucleophiles. This result indicated that the electron-donating ability of carbazole units is much higher than that of other electron-donating groups, which can better promote intramolecular charge transfer.[24e]

The electron excitation process is described as an "electron–hole" transition, and our focus lies on the $S_0 \rightarrow S_1$ transitions of the four oligomeric molecules.[24f] The calculation results are shown in Fig. 4(b), and the detailed calculation data are summarised in Table S1, ESI.† The electron and hole in the S_1 excited state are mainly confined to the electron-absorbing unit DPP, indicating that the absorbed energy undergoes significant ICT, which facilitates the increase of carrier mobility. From a practical standpoint for **Flu(DPPFlu)$_2$**, the distance index between the hole and the electron centre (D) is only 0.31 Å, Sr is large (0.82 Å > 0.5 Å) and the $\Delta\sigma$ index is not large (0.233 Å), so it can be judged that the excitation of $S_0 \rightarrow S_1$ is LE (local excitation). After the structural regulation, the introduction of alkoxyphenyl led to the synthesis of the oligomer **BPF(DPPBPF)$_2$**, and the analysis of its $S_0 \rightarrow S_1$ leap shows that both the D (2.99 Å) and Sr (0.81 Å > 0.5 Å) are large; the excitation shifts to CT (charge transfer excitation), indicating that the electron and hole overlap is significantly reduced. Then, aiming to enhance the electron-donating ability of the material, the end groups were replaced with carbazole units and the overall spatial distribution breadth ($\Delta\sigma$) increased significantly from 0.122 Å to 1.142 Å, implying that a better separation of the electrons and holes was achieved. Finally, the oligomer **Cz(DPPCz)$_2$** with a coulomb attraction energy of only 2.02 eV, favors the suppression of the exciton combination and facilitates carrier migration. The oligomeric molecular structures exhibit an exceptional distribution of electrons and holes in the excited state, as indicated by the aforementioned electron–hole analysis, rendering them highly suitable for applications in organic photovoltaic materials.[24g]

Optical properties

The spectral absorption range and intensity of the materials are important factors affecting the photoelectric conversion efficiency of photovoltaic devices. The UV-vis absorption spectra of all the oligomer-like materials in dilute chloroform solution and thin film state were experimentally studied. As shown in Fig. 5, the maximum absorption wavelengths of **Flu(DPPFlu)$_2$**, **BPF(DPPBPF)$_2$**, **BPF(DPPCz)$_2$**, and **Cz(DPPCz)$_2$** are 644, 647, 636, and 652 nm, corresponding to molar extinction coefficient (ε) values are 1.05×10^5, 0.99×10^5, 1.09×10^5, and 1.24×10^5 M^{-1} cm^{-1}, respectively. Compared with small molecules composed of the same repeating units, the spectral absorption range of the oligomer-like molecules is broadened, which is very favorable for the improvement of the photoelectric performance.[21b,25] Among these oligomer-like materials, **Cz(DPPCz)$_2$** shows the largest ε value and achieves the widest absorption range, which is conducive to improving the photon absorption efficiency. In the solid-state thin film state, due to the strong intermolecular π–π interactions, the maximum absorption peaks of the four materials have undergone redshifts of 16, 11, 30, and 31 nm, respectively. A large redshift is more conducive to the capture of photons by the material, thereby contributing to the improvement of the J_{sc} of the device. In addition, the optical band gaps (E_g^{opt}) (E_g^{opt} = 1240/λ_{edge}^{film}) calculated based on the corresponding band edge values of the thin film are 1.75 eV, 1.72 eV, 1.66 eV, and 1.63 eV, respectively, realizing the design concept of narrow band gaps for oligomer-like materials, consistent with the trend of theoretical calculations.

To obtain more information on the molecular aggregation properties of the oligomer-like molecules, the temperature-dependent absorption spectra of **Flu(DPPFlu)$_2$**, **BPF(DPPBPF)$_2$**, **BPF(DPPCz)$_2$**, and **Cz(DPPCz)$_2$** in *o*-dichlorobenzene solution were studied, as shown from the data in Fig. 6, and the variation values are shown in Table S4 in ESI.† As the temperature increases from 30 to 80 °C, the absorption intensities of the maximum absorption peaks at $A_{0\text{-}1}$ of the four compounds show a slight decrease with a slight blue shift in the wavelength. This observation is consistent with the fact that higher temperatures produce a greater degree of

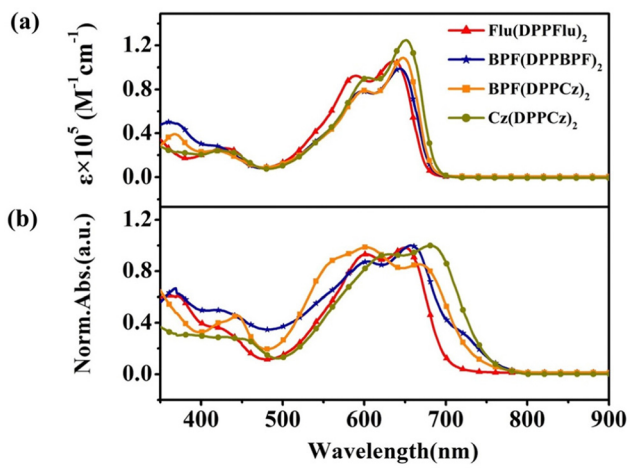

Fig. 5 Spectral characteristics of the four compounds: (a) UV-Vis absorption spectra in $CHCl_3$ solution; (b) normalized UV-Vis absorption spectra in thin film state.

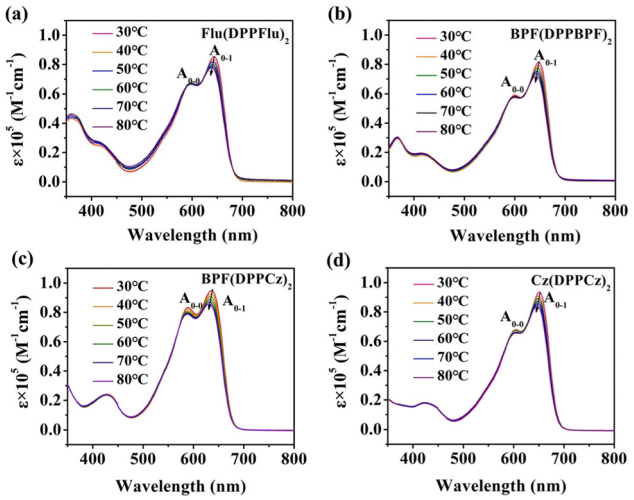

Fig. 6 Temperature-dependent absorption spectra of (a) **Flu(DPPFlu)$_2$**, (b) **BPF(DPPBPF)$_2$**, (c) **BPF(DPPCz)$_2$**, and (d) **Cz(DPPCz)$_2$** in dilute *o*-dichlorobenzene solutions at a temperature interval of 10 °C.

disorder in the molecules, which means that, in many cases, these molecules may tend to aggregate at relatively low temperatures.[26] In fact, a significant red shift in the absorption spectrum of the thin film state compared to the absorption in the solution is sufficient to indicate a strong intermolecular π–π stacking interaction in the solid state. Here, the slight change of the absorption peak with temperature proves the relationship between the intermolecular force and temperature and also proves the thermal stability of the materials.[25d] Furthermore, to showcase the photostability of the oligomeric materials, the UV-Vis spectra of the films were analyzed under light aging conditions in an environmental chamber without encapsulation. All the materials were stored under continuous illumination equivalent under the extended light illumination at 100 mW cm^{-2} in air and data were collected from 1 h to 12 h. As shown in Fig. S19 (ESI†), all oligomer-like materials showed no significant red or blue shifts in the UV-vis absorption spectra and hardly any changes in the molar extinction coefficient (ε) value were observed after long periods of light exposure, indicating the high photostability of the oligomer-like materials, which will help to slow down the ageing of oligomer-based devices. However, the diffusion of the carriers' transport layers and electrodes can change the energy levels of each layer and cause traps, which accelerate the non-radiative charge recombination and reduce the photostability of the device.[28e,29]

Electrochemical properties

The electrochemical properties of the materials were studied using cyclic voltammetry (CV), as shown in Fig. 7(a). The redox properties of the compounds were analyzed in detail, and the electrochemical energy levels and band gaps were obtained. The reduction potential (E_{red}) and oxidation potential (E_{ox}) in the curves of **Flu(DPPFlu)$_2$**, **BPF(DPPBPF)$_2$**, **BPF(DPPCz)$_2$**, and **Cz(DPPCz)$_2$** were −1.21/0.35 V, −1.07/0.43 V, −1.09/0.33 V, and −1.12/0.20 V, respectively. Then, according to the empirical equation: $E^{CV}_{HOMO}/E^{CV}_{LUMO} = -(E_{ox}/E_{red}\text{-}E_{Fc/Fc+}{}^{1/2} + 4.8)$ eV and the $E_{Fc/Fc+}{}^{1/2}$ was 0.05 V (*vs.* Ag/Ag$^+$). The HOMO and LUMO energy levels calculated from the oxidation and reduction potentials were −5.10/−3.54 eV, −5.18/−3.68 eV, −5.08/−3.66 eV, and −4.95/−3.63 eV, respectively. From the above data, it is concluded that **Cz(DPPCz)$_2$** has the narrowest band gap of 1.32 eV. In addition, the matching degree between the donor and acceptor in the device's active layer is also directly related to the diffusion and separation of excitons, which determines the level of the photoelectric conversion efficiency. As shown in Fig. 7(b), when $PC_{71}BM$ is used as an acceptor, the LUMO energy level difference between the four materials and the

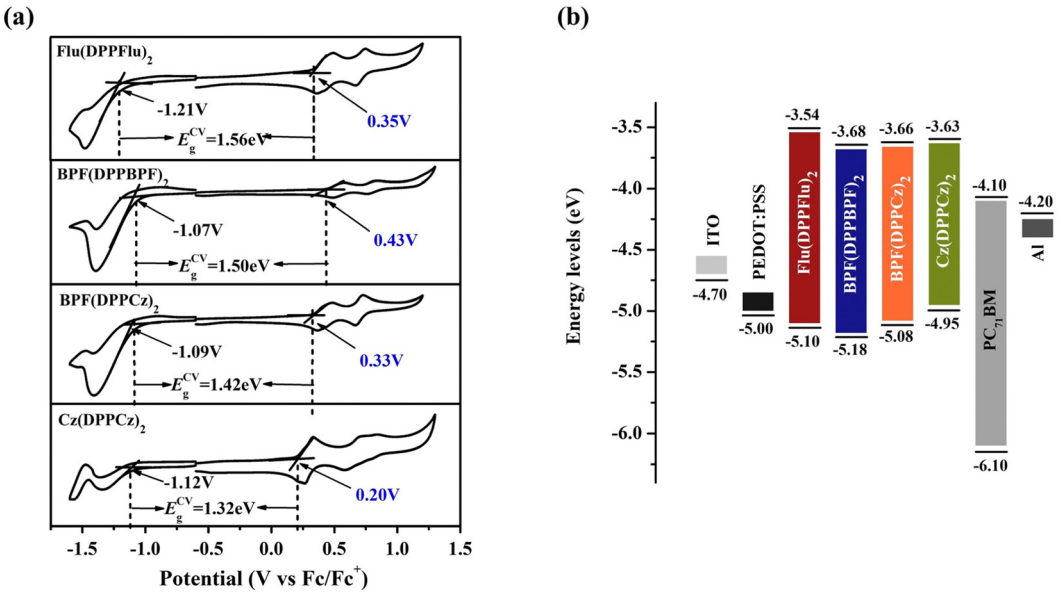

Fig. 7 Electrochemical cyclic voltammetry curves and energy levels: (a) CV curves of **Flu(DPPFlu)$_2$**, **BPF(DPPBPF)$_2$**, **BPF(DPPCz)$_2$**, and **Cz(DPPCz)$_2$** in 0.1 M Bu_4NBF_4/CH_2Cl_2 solution at a scan rate of 100 mV s^{-1} under nitrogen atmosphere; (b) energy level diagram of the four materials and $PC_{71}BM$.

acceptor is greater than 0.3 eV, which is sufficient for the charge separation at the donor–acceptor interface. The electrochemical results show that introducing alkoxyphenyl into the weak electron donor unit of **Flu(DPPFlu)$_2$** to obtain **BPF(DPPBPF)$_2$** can effectively reduce the HOMO energy level, which is conducive to generating relatively high V_{oc} in the device.[27] Compared to other related materials, the oligomer-like compound **Cz(DPPCz)$_2$** synthesized in this study, with a relatively strong electron-donating unit carbazole and an electron-withdrawing unit DPP as periodic segments, exhibits the narrowest band gap. Table S3 in ESI† also provides detailed comparative data on the electrochemical energy levels and photovoltaic performance of other related small molecules.[27b] The improvement of the oligomer-like molecular skeleton extends the conjugation of molecules, significantly reduces the band gap, and broadens light absorption. Therefore, it shows a broad development space in the field of organic photovoltaic materials.

Photovoltaic properties

To evaluate the photovoltaic (PV) properties of all oligomer-like molecular donors (OMDs), BHJ devices based on **Flu(DPPFlu)$_2$**, **BPF(DPPBPF)$_2$**, **BPF(DPPCz)$_2$**, and **Cz(DPPCz)$_2$** were fabricated using a conventional structure of ITO/PEDOT:PSS/OMDs:$PC_{71}BM$ (w/w, 1 : 2)/Al. The current–voltage (J–V) characteristics and PV parameters are shown in Fig. 8(a) and Table 2. Firstly, spin-coated devices based on **Flu(DPPFlu)$_2$**/$PC_{71}BM$ blend film provided PCE of 2.37% with a V_{oc} of 0.87 V, which was still slightly higher than the reported PCE for small molecule **DPP(Flu)$_2$** with the same periodic repeating segments.[21b] Then, the electron-donating unit of **Flu(DPPFlu)$_2$** was modified with alkoxyphenyl side chain groups to obtain **BPF(DPPBPF)$_2$**. Conventional devices using **BPF(DPPBPF)$_2$**/$PC_{71}BM$ as the active layer gave a PCE of 4.28% with a higher V_{oc} of 0.94 V. However, as another important parameter for characterizing photovoltaic devices, J_{sc} is limited to 12.95 mA cm^{-2}, which requires further optimization to ultimately improve the PCE of the device, thereby enabling oligomer-like materials to have a bright future. Subsequently, the terminal spirobifluorene group in the oligomer-like molecule **BPF(DPPBPF)$_2$** is replaced by a carbazole unit to obtain **BPF(DPPCz)$_2$**. The results are consistent with the design concept, achieving an increased J_{sc} of 14.17 mA cm^{-2} and an improved PCE of 4.89%. This is due to the strong electron-donating ability of the carbazole units, which can promote ICT and thereby improve the J_{sc} of the

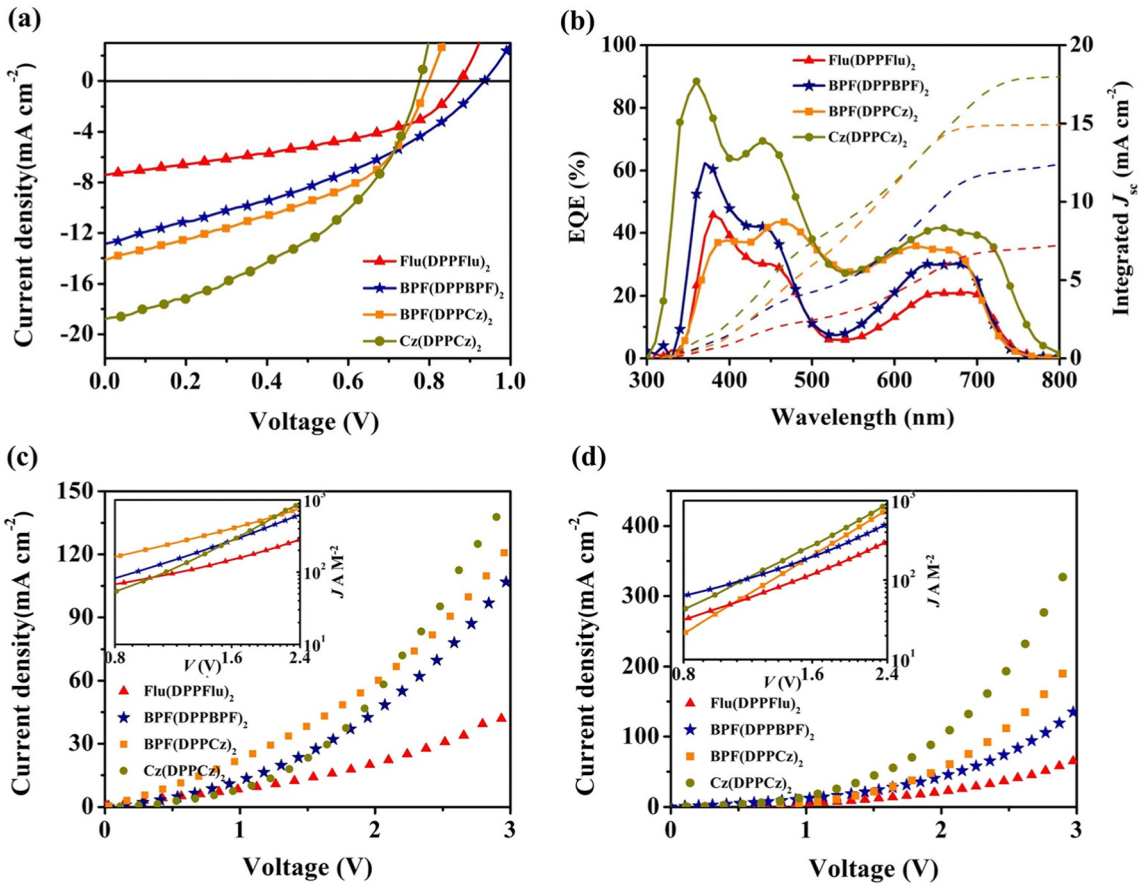

Fig. 8 Photovoltaic properties of the devices based on the organic active layer of **Flu(DPPFlu)$_2$**:$PC_{71}BM$, **BPF(DPPBPF)$_2$**:$PC_{71}BM$, **BPF(DPPCz)$_2$**:$PC_{71}BM$, and **Cz(DPPCz)$_2$**:$PC_{71}BM$. (a) J–V curves; (b) EQE spectra with the integrated current curves of the devices; (c) J–V curves for the hole-only devices; and (d) J–V curves for the electron-only devices. Inset: The J–V plots in a double logarithmic scale, where the solid line is the fitting of data points to the SCLC model.

Table 2 Photovoltaic data of the devices based on the organic active layer with **Flu(DPPFlu)$_2$**:$PC_{71}BM$, **BPF(DPPBPF)$_2$**:$PC_{71}BM$,**BPF(DPPCz)$_2$**:$PC_{71}BM$, and **Cz(DPPCz)$_2$**:$PC_{71}BM$

Organic active layer of devices	μ_h ($cm^2\ V^{-1}\ s^{-1}$)	μ_e ($cm^2\ V^{-1}\ s^{-1}$)	μ_h/μ_e	V_{OC} (V)	J_{SC} (mA cm^{-2})	J_{SC}^{cal} A (cm^{-2})	FF	PCE (PCE$_{ave}$) (%)
Flu(DPPFlu)$_2$:$PC_{71}BM$	9.23×10^{-5}	2.78×10^{-5}	3.32	0.87	7.40	7.29	0.368	2.37 (2.15)
BPF(DPPBPF)$_2$:$PC_{71}BM$	4.37×10^{-4}	1.43×10^{-4}	3.06	0.94	12.95	12.43	0.352	4.28 (4.11)
BPF(DPPCz)$_2$:$PC_{71}BM$	5.02×10^{-4}	2.26×10^{-4}	2.22	0.81	14.17	14.82	0.426	4.89 (4.44)
Cz(DPPCz)$_2$:$PC_{71}BM$	6.82×10^{-4}	4.16×10^{-4}	1.64	0.79	18.16	17.89	0.427	6.12 (6.08)

The average data of PCE were obtained from 24 devices.

device.[28] Finally, **Cz(DPPCz)$_2$** was constructed as an oligomer-like donor material using Cz-DPP as a periodic repeat. As expected, a relatively high PCE of 6.12% was obtained, accompanied by a J_{sc} of 18.16 mA cm^{-2}. Compared to the previously reported small molecules DPP(Cz)$_2$ with the same periodic repeating segments,[21b] the PCE was increased by more than four times. The improved circuit and efficiency are attributed to the rational molecular design of oligomers. In short, the above photovoltaic experimental results are consistent with the material design ideas and theoretical calculation simulation. The precise regulation of the specific electron-donating units of the oligomers provides a simple and promising strategy for developing novel OSC donor materials.[28b] Furthermore, the *J–V* characteristics under photo-aging conditions at 100 mW cm^{-2} in the air of **Flu(DPPFlu)$_2$**/**BPF(DPPBPF)$_2$**/**BPF(DPPCz)$_2$**/**Cz(DPPCz)$_2$**:$PC_{71}BM$-based devices were monitored to determine the device's photostability. The normalized J_{sc}, V_{oc}, PCE, and FF expressed as a function of light soaking time is shown in Fig. S20 (ESI†). The photostability of the oligomer materials-based devices decreased during 30 min of photoaging at room temperature (r.t.), retaining 80% of their original PCE, which indicates that the device is relatively stable in a short time. However, after a few hours of photo-ageing, the PCE decays significantly, which is the result of a significant reduction in short-circuit current. The photostability of these devices is not as good as those reported for some of the high-efficiency and high-stability devices,[28f] which mainly stems from the burn-in degradation of electrodes and interfaces or the photooxidation of the active layer and the carrier transport layer in most of the cases.[29f–h]

External quantum efficiency (EQE)

The photoelectric conversion process was further studied using the external quantum efficiency (EQE) spectra of the devices. As a result, EQE spectra with the integrated current curves are shown in Fig. 8(b). Obviously, all oligomer-like materials exhibit two important photoelectric characteristic response regions. In the high-energy region (300–500 nm), **Flu(DPPFlu)$_2$**-based devices exhibit two shoulder peaks with maximum EQE values of 45.96% and 25.85%, while in the low-energy region (500–800 nm), the device has a maximum EQE of 21.20%. With the optimization of the chemical structure, the maximum EQE values of the devices based on **BPF(DPPBPF)$_2$** are significantly enhanced, with the maximum EQE values of 62.11% and 44.98% in the high-energy region, and 30.07% in the low-energy region. With further optimization of the terminal group, the maximum EQE values of devices based on **BPF(DPPCz)$_2$** in the high-energy region were 37.56% and 43.88%, with no significant changes, but slightly increased to 35.69% in the low-energy region. Finally, the devices based on the oligomer-like molecules **Cz(DPPCz)$_2$** exhibited the highest EQE values, reaching 88.78% and 69.45% in the high-energy region, and 41.77% in the low-energy region, consistent with its relatively strong and wide absorption spectrum. These results demonstrate that with the gradual optimization of the chemical structure, the external quantum efficiency was effectively improved, and of course, the J_{sc} of the device was also increased. According to the EQE spectrum, the integrated current (J_{sc}^{cal}) values of the devices based on **Flu(DPPFlu)$_2$**, **BPF(DPPBPF)$_2$**, **BPF(DPPCz)$_2$**, and **Cz(DPPCz)$_2$** were 7.29 mA cm^{-2}, 12.43 mA cm^{-2}, 14.82 mA cm^{-2} and 17.89 mA cm^{-2}, respectively. The relevant data are shown in Table 2, which are very consistent with the J_{sc} obtained from their *J–V* curves (less than 5% error). Obviously, the devices based on oligomer-like molecule **Cz(DPPCz)$_2$** exhibited the highest EQE and the largest J_{sc}, which is closely related to its strong and wide light absorption and inevitably leads to an improvement in the photoelectric conversion efficiency.[29]

Charge carrier mobility

The charge transport properties were studied using the space-charge-limited current (SCLC) method. The hole mobility (μ_h) and electron mobility (μ_e) of all OMDs are discussed in detail by preparing the hole-only devices of ITO/PEDOT:PSS/OMDs:$PC_{71}BM$/Au and electron-only devices of ITO/ZnO/OMDs:$PC_{71}BM$/Al. The corresponding charge carrier mobility data and *J–V* curves are shown in Table 2 and Fig. 8(c and d). The μ_h values of devices based on **Flu(DPPFlu)$_2$**, **BPF(DPPBPF)$_2$**, **BPF(DPPCz)$_2$** and **Cz(DPPCz)$_2$** were obtained using the Mott-Gurney law (details are given in ESI†), and the μ_h values are 9.23×10^{-5}, 4.37×10^{-4}, 5.02×10^{-4} and 6.82×10^{-4} $cm^2\ V^{-1}\ s^{-1}$, with the corresponding μ_e values of 2.78×10^{-5}, 1.43×10^{-4}, 2.26×10^{-4}, and 4.16×10^{-4} $cm^2\ V^{-1}\ s^{-1}$, respectively. From the experimental results, it is known that with the optimization of the molecular structure, both the electron mobility and the hole mobility were improved, which is the fundamental reason for the improvement of the J_{sc} and FF. Furthermore, well-balanced carrier mobility can also reduce charge recombination and increase the J_{sc} and FF of the photovoltaic devices. The ratios of μ_h/μ_e for the devices based on the four materials were 3.32, 3.06, 2.22, and 1.64 respectively. It is obvious that the device based on **Cz(DPPCz)$_2$** exhibits higher electron and hole mobility and is well-balanced at μ_h and μ_e. This confirms once again that the most effective carrier transport occurs in the **Cz(DPPCz)$_2$**:$PC_{71}BM$ blend film, and achieves the highest J_{SC} and PCE among the four materials.[30]

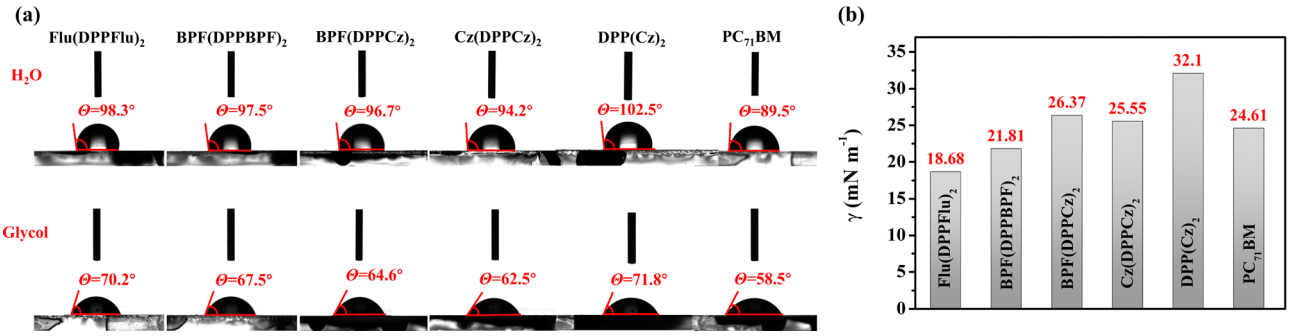

Fig. 9 (a) Contact angle images of water and ethylene glycol droplets for **Flu(DPPFlu)$_2$**, **BPF(DPPBPF)$_2$**, **BPF(DPPCz)$_2$**, **Cz(DPPCz)$_2$**, **DPP(Cz)$_2$** and PC$_{71}$BM on ITO/glass substrates; (b) surface energy histogram of different photovoltaic materials.

Contact angle and surface tension

The ideal morphology of the active layer blend film is formed by donors and acceptors with similar surface tension values. To understand the interfacial properties of the four materials and their compatibility with acceptors, the contact angle was measured using a dual solvent method (deionized water and ethylene glycol). As shown in Fig. 9(a) and Table S4 in ESI,† the contact angles measured with deionized water for the five materials were 98.3°, 97.5°, 96.7°, 94.2°, and 89.5° for **Flu(DPPFlu)$_2$**, **BPF(DPPBPF)$_2$**, **BPF(DPPCz)$_2$**, **Cz(DPPCz)$_2$**, and PC$_{71}$BM, respectively. When using ethylene glycol as a solvent, the measured contact angles were 70.2°, 67.5°, 64.4°, 62.5°, and 58.5°, respectively. It is obvious that the hydrophilicity of the four materials increases in turn. Due to the presence of carboxylic acid groups, the acceptor PC$_{71}$BM exhibits the best hydrophilicity. Using contact angle measurements, the surface tension (γ) values of the four materials were calculated[1c,31] to be 18.68, 21.81, 26.37, and 25.55 mN m^{-1}, respectively. The value of the neat PC$_{71}$BM film was 24.61 mN m^{-1}, as shown in Fig. 9(b), indicating that the γ value of **Cz(DPPCz)$_2$** is closest to that of PC$_{71}$BM. Moreover, the Flory-Huggins interaction parameter (χ) is used to evaluate the miscibility of the active layer material. It is reported that the lower the value of χ, the better the miscibility of the donor and acceptor materials.[32] Then, according to the Flory-Huggins interaction model ($\chi \approx K\left(\sqrt{\gamma_D} - \sqrt{\gamma_A}\right)^2$) the calculated Flory–Huggins interaction parameters for different active layers **Flu(DPPFlu)$_2$**:PC$_{71}$BM, **BPF(DPPBPF)$_2$**:PC$_{71}$BM, **BPF(DPPCz)$_2$**:PC$_{71}$BM, and **Cz(DPPCz)$_2$**:PC$_{71}$BM were 0.4, 0.08, 0.03, and 0.009 K, respectively.[1c,31,32] By comparison, the calculated χ value of **Cz(DPPCz)$_2$**:PC$_{71}$BM (0.009 K) is much smaller than that of the others, indicating that **Cz(DPPCz)$_2$**, as a component of the electron donor, has better miscibility with the PC$_{71}$BM acceptor; this will help to form a more favourable active layer morphology in PV devices, which is also an important reason why **Cz(DPPCz)$_2$**-based devices display higher PCE. Furthermore, to demonstrate the superiority of the oligomer molecule structure, we measured the contact angles of DPP(Cz)$_2$ with the two solvents: water (102.5°) and ethylene glycol (71.8°) with a surface tension of 32.1 mN m^{-1} and a calculated χ value of 0.498, which are bigger than that of all the oligomeric molecules synthesised in this work. It appears that OMDs are more compatible with PC$_{71}$BM acceptors than SMDs, which provides evidence for the superior optoelectronic properties resulting from extended conjugation.

Conclusions

In summary, a series of novel oligomer-like molecules **Flu(DPPFlu)$_2$**, **BPF(DPPBPF)$_2$**, **BPF(DPPCz)$_2$**, and **Cz(DPPCz)$_2$** were successfully synthesized by the Suzuki coupling reaction. The theoretical calculation and detailed study of the photoelectric properties of the above materials proved that all oligomer-like molecules exhibited high chemical and photostability. The molecular design and structural regulation have a significant effect on their photovoltaic properties. In the first stage, the alkoxyphenyl groups were introduced into **Flu(DPPFlu)$_2$** through the terminal group and the side chain regulation, and the oligomer-like material **BPF(DPPBPF)$_2$** was obtained, which reduced the HOMO level and expanded the molecular conjugation, resulting in an increase of V_{oc} in the device to 0.94 V. In the second stage, **BPF(DPPCz)$_2$** was synthesized by introducing a carbazole rigid terminal unit with a stronger electron-donating ability. As an excellent electronic donor unit, carbazole not only ensured the planarity of the molecule but also promoted the intramolecular ICT process, so that J_{sc} reached 14.17 mA cm^{-2}. Finally, an oligomer-like donor material **Cz(DPPCz)$_2$** with carbazole as both the central core and the terminal unit was synthesized, with a narrow band gap of 1.32 eV. The PCE of the devices using PC$_{71}$BM as the acceptor reached 6.12%, which was three times higher than that reported previously for the small molecule counterpart DPP(Cz)$_2$ with a PCE of only 1.48%. The relationship between the structure regulation and charge conduction mechanism was discussed in detail. In highly conjugated oligomer-like molecules, both the increase in the photon capture and the formation and dissociation of high-energy excitons were promoted. By comparing the experimental results, the devices based on oligomer-like molecule **Cz(DPPCz)$_2$** exhibited the highest EQE and maximum J_{sc}, as well as a good balance of the higher electron and hole mobility. In addition, the calculated χ value of **Cz(DPPCz)$_2$**:PC$_{71}$BM is much lower than that of the others, indicating that **Cz(DPPCz)$_2$**, as a component of the electron donor, has better compatibility with the acceptor PC$_{71}$BM. These results not only confirmed that the most effective carrier transport occurs in the **Cz(DPPCz)$_2$**:PC$_{71}$BM blend film but

also helped to form the most favourable morphology in PV devices, which is an important reason why devices based on **Cz(DPPCz)$_2$** show higher PCE. We believe that the structural design and regulation of the oligomer-like donor materials have great potential, and our research provides experimental and theoretical references for the development of novel oligomer-like photovoltaic materials with excellent photoelectric properties.

Conflicts of interest

There are no conflicts to declare.

Acknowledgements

We are grateful for the support of the National Natural Science Foundation (No. 21102013) and the Fundamental Funds for the Central Universities (DUT16ZD205).

Notes and references

1 (*a*) G. D. Sharma, R. Pradhan, K. Khandelwal, R. Singhal, W. Liu, X. Zhu and A. Mishra, *J. Mater. Chem. C*, 2023, **11**, 1919–1926; (*b*) J. Ge, Z. Chen, Q. Ye, L. Xie, W. Song, Y. Guo, J. Zhang, X. Tong, J. Zhang, E. Zhou, Z. Wei and Z. Ge, *ACS Appl. Mater. Interfaces*, 2023, **15**, 10803–10811; (*c*) C. Liu, Z. Wu, N. Qiu, C. Li and Y. Lu, *ACS Appl. Mater. Interfaces*, 2023, **15**, 9764–9772; (*d*) Q. Yang, D. Hu, M. Kumar, H. Dong, S. Ahmed, P. Huang, Z. Xiao and S. Lu, *Solar RRL*, 2023, **215**, 111279; (*e*) C. Zhang, J. Li, L. Ji, H. Hu, G. Li and K. Wang, *J. Mater. Chem. A*, 2022, **10**, 22812–22818.

2 Y. Cui, Y. Xu, H. Yao, P. Bi, L. Hong, J. Zhang, Y. Zu, T. Zhang, J. Qin, J. Ren, Z. Chen, C. He, X. Hao, Z. Wei and J. Hou, *Adv. Mater.*, 2021, **33**, e2102420.

3 (*a*) M. Kankanan, A. Kosarian and E. Farshidi, *J. Mater. Sci.: Mater. Electron.*, 2018, **29**, 12387–12398; (*b*) A. Foertig, J. Kniepert, M. Gluecker, T. Brenner, V. Dyakonov, D. Neher and C. Deibel, *Adv. Funct. Mater.*, 2014, **24**, 1306–1311; (*c*) R. Hu, X. Su, H. Liu, Y. Liu, M.-M. Huo and W. Zhang, *J. Mater. Sci.*, 2020, **55**, 11403–11410; (*d*) C. Zhou, R. Hu, Y. Liu, M.-M. Huo, L. Li and J. Yu, *Org. Electron.*, 2020, **83**, 105753.

4 (*a*) H. Chen, H. Liang, Z. Guo, Y. Zhu, Z. Zhang, Z. Li, X. Cao, H. Wang, W. Feng, Y. Zou, L. Meng, X. Xu, B. Kan, C. Li, Z. Yao, X. Wan, Z. Ma and Y. Chen, *Angew. Chem., Int. Ed.*, 2022, **61**, e202209580; (*b*) H. Chen, Y. Zou, H. Liang, T. He, X. Xu, Y. Zhang, Z. Ma, J. Wang, M. Zhang, Q. Li, C. Li, G. Long, X. Wan, Z. Yao and Y. Chen, *Sci. China: Chem.*, 2022, **65**, 1362–1373; (*c*) J. Wang and X. Zhan, *Acc. Chem. Res.*, 2021, **54**, 132–143; (*d*) S. He, Z. Lin, F. Du, X. Wang, Y. Liu and W. Tang, *Chem. Eng. J.*, 2022, **441**, 135973; (*e*) M. Chang, Y. Zhang, B.-S. Lu, D. Sui, F. Wang, J. Wang, Y. Yang and B. Kan, *Chem. Eng. J.*, 2022, **427**, 131473; (*f*) T. Duan, Q. Yang, Z. Sun, Q. Chen, G. Zhang, D. Hu, J. Oh, C. Yang, J. Lv, B. Feng, Z. Kan, S. Chen, C. Zhong, S. Lu and K. Yang, *Chem. Eng. J.*, 2023, **456**, 141006.

5 J. Ge, L. Hong, H. Ma, Q. Ye, Y. Chen, L. Xie, W. Song, D. Li, Z. Chen, K. Yu, J. Zhang, Z. Wei, F. Huang and Z. Ge, *Adv. Mater.*, 2022, **34**, e2202752.

6 U. Ali, H. Etabti, H. M. R. Ahmad and S. U. Zafar, *J. Phys. Chem. C*, 2022, **1215**, 113831.

7 K. M. Katubi, A. M. S. Pembere, M. Y. Mehboob and M. S. Al-Buriahi, *Int. J. Quantum Chem.*, 2022, **122**, e26998.

8 (*a*) L. Luo, X. Chi, L. Wu, L. Ren, J. Lin, Y. Zhang and M.-H. Zeng, *Synth. Met.*, 2021, **276**, 116759; (*b*) Y. Lin and X. W. Zhan, *Acc. Chem. Res.*, 2016, **49**, 175–183; (*c*) F. G. Guijarro, P. Malhotra, G. Gupta, R. Caballero and F. Langa, *J. Mater. Chem. C*, 2020, **8**, 4763–4770; (*d*) R. Fitzner, E. Mena-Osteritz, A. Mishra, G. Schulz, E. Reinold and P. Baüerle, *J. Am. Chem. Soc.*, 2012, **134**, 11064–11067.

9 H. Xia, X. Xu, C. Qian, J. Guo, J. Zhao, K. Zhang, H. Tan, Q. Peng and W. Zhu, *ACS Appl. Energy Mater.*, 2022, **5**, 3146–3155.

10 Y. Liang, D. Zhang, Z. Wu, T. Jia, L. Lüer, H. Tang, L. Hong, J. Zhang, K. Zhang, C. J. Brabec, N. Li and F. Huang, *Nat. Energy*, 2022, **7**, 1180–1190.

11 H. Xia, Y. Zhang, W. Deng, K. Liu, X. Xia, C. J. Su, U. S. Jeng, M. Zhang, J. Huang, J. Huang, C. Yan, W. Y. Wong, X. Lu, W. Zhu and G. Li, *Adv. Mater.*, 2022, **34**, e2205638.

12 (*a*) B. Li, H. Yu, E. C. Montoto, Y. Liu, S. Li, K. Schwieter, J. Rodríguez-López, J. S. Moore and C. M. Schroeder, *ACS Appl. Electron. Mater.*, 2018, **1**, 7–12; (*b*) T. E. Anderson, E. W. Culver, I. Badia-Dominguez, W. D. Wilcox, C. E. Buysse, M. C. Ruiz Delgado and S. C. Rasmussen, *Phys. Chem. Chem. Phys.*, 2021, **23**, 26534–26546; (*c*) S. René, D. Françoise, G. Issaka, O. Raguilnaba and S. Jean-Marc, *J. Am. Chem. Soc.*, 2016, **17**, 1–10; (*d*) A. Borchers and T. Pieler, *Genes*, 2010, **1**, 413–426; (*e*) A. L. Mannanov, P. S. Savchenko, Y. N. Luponosov, A. N. Solodukhin, S. A. Ponomarenko and D. Y. Paraschuk, *Org. Electron.*, 2020, **78**, 105588; (*f*) D. Sahu, A. K. Kar, A. K. Pattanaik, P. S. R. Sreekanth and N. D. Badgayan, *SN Appl. Sci.*, 2018, **1**, 29; (*g*) H. Xia, X. Xu, J. Guo, C. Qian, K. Zhang, M. Zhu, B. Zhang, W. Peng, Q. Peng and W. Zhu, *Dyes Pigm.*, 2021, **186**, 108950; (*h*) W. Wang and S. Zheng, *Int. J. Quantum Chem.*, 2020, **120**, e26066; (*i*) F. G. Guijarro, P. Malhotra, G. Gupta, R. Caballero, P. de la Cruz, R. Singhal, G. D. Sharma and F. Langa, *J. Mater. Chem. C*, 2020, **8**, 4763–4770.

13 L. Fu, H. Hu, Q. Zhu, L. Zheng, Y. Gu, Y. Wen, H. Ma, H. Yin and J. Ma, *Nano Res.*, 2022, **16**, 3588–3596.

14 H. Wang, C. Cao, H. Chen, H. Lai, C. Ke, Y. Zhu, H. Li and F. He, *Angew. Chem., Int. Ed.*, 2022, **61**, e202201844.

15 T. Matsumoto, T. Murakami, F. Schlüter, H. Murata, V. Vohra and F. Rizzo, *Solar RRL*, 2021, **6**, 2100661.

16 X. Chen, C. Liao, M. Deng, X. Xu, L. Yu, R. Li and Q. Peng, *Chem. Eng. J.*, 2023, **451**, 139046.

17 B. Xie, L. Yin, J. Fan, C. Liu and Y. Li, *J. Mater. Chem. C*, 2022, **10**, 3248–3258.

18 (*a*) T. P. A. van der Pol, J. Li, B. T. van Gorkom, F. J. M. Colberts, M. M. Wienk and R. A. J. Janssen, *J. Phys. Chem. C Nanomater. Interfaces*, 2021, **125**, 5505–5517; (*b*) M. N. Shah, S. Zhang, Q. Sun, F. Ullah, H. Chen and C. Z. Li, *Tetrahedron*

Lett., 2017, **58**, 2975–2980; (*c*) W. Sun, Y. Zheng, Q. Zhang, K. Yang, H. Chen, Y. Cho, J. Fu, O. Odunmbaku, A. A. Shah, Z. Xiao, S. Lu, S. Chen, M. Li, B. Qin, C. Yang, T. Frauenheim and K. Sun, *J. Phys. Chem. Lett.*, 2021, **12**, 8847–8854; (*d*) R. Feng, N. Sato, T. Yasuda, H. Furuta and S. Shimizu, *Chem. Commun.*, 2020, **56**, 2975–2978; (*e*) X. Song, N. Gasparini, M. M. Nahid, S. H. K. Paleti, C. Li, W. Li, H. Ade and D. Baran, *Adv. Funct. Mater.*, 2019, **29**, 1902441; (*f*) K. Sun, X. Tang, Y. Ran, R. He, W. Shen and M. Li, *Phys. Chem. Chem. Phys.*, 2018, **20**, 1664–1672; (*g*) K. Kranthiraja, K. Murotani, F. Hamada and A. Saeki, *ACS Appl. Electron. Mater.*, 2022, **4**, 2086–2094; (*h*) Y. Wang, T. Wang, J. Chen, H. D. Kim, P. Gao, B. Wang, R. Iriguchi and H. Ohkita, *Dyes Pigm.*, 2018, **158**, 213–218; (*i*) R. Shivhare, T. Erdmann, U. Hörmann, E. Collado-Fregoso, S. Zeiske, J. Benduhn, S. Ullbrich, R. Hübner, M. Hambsch, A. Kiriy, B. Voit, D. Neher, K. Vandewal and S. C. B. Mannsfeld, *Chem. Mater.*, 2018, **30**, 6801–6809; (*j*) Y. Patil and R. Misra, *J. Mater. Chem. C*, 2019, **7**, 13020–13031.

19 (*a*) M. A. Marsya, D. Hayati, S. Han, D. X. Long, K. Choi and J. Hong, *Dyes Pigm.*, 2022, **200**, 110131; (*b*) S. Pıravadılı, C. Doyranlı, S. Altınısık, H. Bilgili, B. Canımkurbey and S. Koyuncu, *J. Polym. Sci.*, 2021, **59**, 1829–1840; (*c*) Q. Yang, Z. Hu, S. Zhu, R. Ma, H. Ma, Z. Ma, H. Wan, T. Zhu, Z. Jiang, W. Liu, L. Jiao, H. Sun, Y. Liang and H. Dai, *J. Am. Chem. Soc.*, 2018, **140**, 1715–1724; (*d*) R. F. B. Nasrun, D. H. Son, S. A. Salma and J. H. Kim, *Dyes Pigm.*, 2022, **206**, 110625.

20 J. Hofinger, S. Weber, F. Mayr, A. Jodlbauer, M. Reinfelds, T. Rath, G. Trimmel and M. C. Scharber, *J. Mater. Chem. A Mater.*, 2022, **10**, 2888–2906.

21 (*a*) Y. Chen, L. Hu, Z. Su, X.-F. Zhang, H. Liu, L.-H. Wang, B. Huang, Z. Li and S.-Y. Liu, *ACS Appl. Polym. Mater.*, 2022, **4**, 1940–1947; (*b*) C. Ji, L. Yin, K. Li, L. Wang, X. Jiang, Y. Sun and Y. Li, *RSC Adv.*, 2015, **5**, 31606–31614.

22 (*a*) H. Wang, P.-Y. Gu, H. Li, J.-H. He, J. Jiang, Y. Ji, Y. Li, Q. Xu and J.-M. Lu, *Dyes Pigm.*, 2018, **151**, 28–34; (*b*) M. Li, Z. Li, Z. Yang, Z. Liu, K. Zhang, L. Yang, Q. Peng, W. Zhu and Y. Liu, *Dyes Pigm.*, 2019, **170**, 107595; (*c*) F. Pakpour, E. Safaei, S. M. Azami, A. Wojtczak and K. Kaldunska, *RSC Adv.*, 2023, **13**, 3278–3289; (*d*) J. Pan, L. Wang, W. Chen, S. Sang, H. Sun, B. Wu, X.-C. Hang, Z. Sun and W. Huang, *RSC Adv.*, 2020, **8**, 6749–6755.

23 T. Lu and F. Chen, *J. Comput. Chem.*, 2012, **33**, 580–592.

24 (*a*) L. Wang, L. Yin, L. Wang, B. Xie, C. Ji and Y. Li, *Dyes Pigm.*, 2017, **140**, 203–211; (*b*) M. Afzal, N. Naeem, S. Iqbal, M. S. Al-Buriahi, N. Alfryyan, Z. A. Alrowaili and J. Iqbal, *Opt. Quant. Electron.*, 2022, **55**, 81; (*c*) K. Mohammedsaleh Katubi, M. Saqib, A. Rehman, S. Murtaza, S. Hussain, Z. A. Alrowaili and M. S. Al-Buriahi, *Chem. Phys. Lett.*, 2023, **814**, 140349; (*d*) D. Dodzi Yao Setsoafia, K. Sreedhar Ram, H. Mehdizadeh-Rad, D. Ompong, V. Murthy and J. Singh, *J. Renew. Mater.*, 2022, **10**, 2553–2567; (*e*) L. Wang, J. Ye and Q. Zhang, *Mater. Sci. Semicond. Process.*, 2022, **152**, 107097; (*f*) Z. Y. Liu, T. Lu and Q. X. Chen, *Carbon*, 2020, **165**, 461–467; (*g*) K. Yasuji, T. Sakanoue, F. Yonekawa and K. Kanemoto., *Nat. Commun.*, 2023, **14**, 992.

25 (*a*) M. Lv, Y. Tang, D. Qiu, W. Zou, R. Zhou, L. Liu, Z. Huang, J. Zhang, K. Lu and Z. Wei, *Chin. Chem. Lett.*, 2023, **34**, 107321; (*b*) Z. Li, X. Wang, N. Zheng, A. Saparbaev, J. Zhang, C. Xiao, S. Lei, X. Zheng, M. Zhang, Y. Li, B. Xiao and R. Yang, *Energy Environ. Sci.*, 2022, **15**, 4338–4348; (*c*) R. Zhou, C. Yang, W. Zou, M. Abdullah Adil, H. Li, M. Lv, Z. Huang, M. Lv, J. Zhang, K. Lu and Z. Wei, *J. Energy Chem.*, 2021, **52**, 228–233; (*d*) W. Xu, W. He, G. Li, J. Wu, C. Yang, Z. Cao, P. Cheng, H. Li, Z. Du and D. Yu, *Phys. Chem. Chem. Phys.*, 2023, **25**, 2916–2925; (*e*) L. Zhang, S. Zeng, L. Yin, C. Ji, K. Li, Y. Li and Y. Wang, *New J. Chem.*, 2013, **37**, 632–639.

26 (*a*) M. Li, Z. Qiu, G. Zhang, Y. Liu, L. Xiong, D. Bai, M. Zhu, Q. Peng and W. Zhu, *J. Mater. Chem. A*, 2018, **6**, 12493–12505; (*b*) Y. Yu, N. Wang, B. Meng, J. Liu and L. Wang, *ACS Appl. Polym. Mater.*, 2020, **3**, 42–48; (*c*) X. Gao, R. Yu, X. Song, X. Tao, H. Wang, M. Zhu, Y. Wu, Y. He and Y. Tao, *J. Mater. Chem. C*, 2021, **9**, 7035–7045.

27 (*a*) H. Shen, Y. Ren, J. Li and Y. Xu, *Mol. Cryst. Liq. Cryst.*, 2023, **41**, 644–650; (*b*) D. Neusser, B. Sun, W. L. Tan, L. Thomsen, T. Schultz, L. Perdigón-Toro, N. Koch, S. Shoaee, C. R. McNeill, D. Neher and S. Ludwigs, *J. Mater. Chem. C*, 2022, **10**, 11565–11578.

28 (*a*) S. Jung and Y. Kwon, *Mol. Cryst. Liq. Cryst.*, 2021, **734**, 118–128; (*b*) S. UrRehman, M. Anwer, S. BiBi, S. Jamil, M. Yasin, S. Rauf Khan, R. Nadeem, S. Ali and R. Jia, *Mater. Sci. Semicond. Process.*, 2022, **140**, 106381; (*c*) S. S. Reddy, S. Shin, U. K. Aryal, R. Nishikubo, A. Saeki, M. Song and S.-H. Jin, *Nano Energy*, 2017, **41**, 10–17; (*d*) Y. Q. Zheng, J. L. Yu, W. G. Li, J. Tang, B. Wei, X. F. Li, J. F. Shi, J. H. Zhang and Y. F. Wang, *J. Phys. D: Appl. Phys.*, 2020, **53**, 125102; (*e*) S. Y. Li, X. Yuan, Q. L. Zhang, B. Li, Y. X. Li, J. G. Sun, Y. F. Feng and X. N. Zhang, *Adv. Mater.*, 2021, **33**, 2101295; (*f*) L. P. Duan and A. Uddin, *Adv. Sci.*, 2020, **7**, 1903259.

29 (*a*) Y. Cheng, B. Huang, X. Huang, L. Zhang, S. Kim, Q. Xie, C. Liu, T. Heumuller, Z. Liu, Y. Zhang, F. Wu, C. Yang, C. J. Brabec, Y. Chen and L. Chen, *Angew. Chem. Int. Ed.*, 2022, **61**, e202200329; (*b*) B. Liu, H. L. Sun, J. W. Lee, Z. Y. Jiang, J. Q. Qiao and J. W. Wang, *Nat. Commun.*, 2023, **14**, 967; (*c*) Y. X. Li, B. Huang, X. N. Zhang, J. W. Ding, Y. Y. Zhang and L. G. Xiao, *Nat. Commun.*, 2023, **14**, 1241; (*d*) X. Xu, J. Y. Xiao, G. C. Zhang, L. Wei, X. C. Jiao, H. L. Yip and Y. Cao, *Sci. Bull.*, 2020, **65**, 208–216; (*e*) W. R. Mateker, I. T. Sachs-Quintana, G. F. Burkhard, R. Cheacharoen and M. D. McGehee, *Chem. Mater.*, 2015, **27**, 404–407; (*f*) S. C. Zhang, H. B. Chen, P. Wang, S. Li, Z. X. Li, Y. Z. Huang, J. Liu, Z. Y. Yao, C. X. Li, X. J. Wan and Y. S. Chen, *Sol. RRL*, 2023, **7**, 2300029; (*g*) J. H. Fu, P. W. K. Fong, H. Liu, C. S. Huang, X. H. Lu and M. Abdelsamie, *Nat. Commun.*, 2023, **14**, 1760; (*h*) Z. H. Liu, L. Wang, H. Zhao, P. Chen and X. Y. Xie, *Org. Electron.*, 2023, **120**, 106828.

30 C. Xu, H. Chen, Z. Zhao, J. Gao, X. Ma, S. Lu, X. Zhang, Z. Xiao and F. Zhang, *J. Energy Chem.*, 2021, **57**, 610–617.

31 J. Li, C. Zhang, X. Zhong, W. Deng, H. Hu and K. Wang, *Small*, 2023, **19**, e2205572.

32 M. Guan, W. Tao, L. Xu, Y. Qin, J. Zhang, S. Tan, M. Huang and B. Zhao, *J. Mater. Chem. A*, 2022, **10**, 9746–9752.